FABRICATION AND CHARACTERIZATION OF A MICRO CAPILLARY EVAPORATOR FOR MEMS BASED POWER GENERATION

DANIEL A. CARPENTER

A thesis submitted in partial fulfillment of
the requirements for the degree of

MASTER OF SCIENCE IN MECHANICAL ENGINEERING

WASHINGTON STATE UNIVERSITY
School of Mechanical and Materials Engineering

December 2004

To the Faculty of Washington State University:

The members of the Committee appointed to examine the thesis of DANIEL A. CARPENTER find it satisfactory and recommend that it be accepted.

____
Chair

____

____

ACKNOWLEDGEMENTS

First and foremost, I am deeply grateful for the support from my advisor, Dr. Bob Richards. Without his patient guidance throughout my graduate studies, this research would not have been possible. Although not my main advisor, Dr Cill Richard's enthusiasm for the P^3 project first interested me in graduate research. Her positive outlook and refusal to give up when faced with difficulties are a continued inspiration for my work. Dr. David Bahr faithfully provided assistance with any and all fabrication and processing issues. He was a model of patience while continually teaching techniques and troubleshooting fabrication problems. His hard work and devotion to students did not go unnoticed.

Along with my advisors, the WSU MEMS team provided an excellent atmosphere for both work and camaraderie. Jeanna Kanyer laid the groundwork for my research and was instrumental in passing along her knowledge of the P^3 specifically and MEMS in general. Leland Weiss continually offered insight and expertise for different experimental problems and his design of the RTD testing box was invaluable for the use of RTDs in my experiments. Scott Whalen worked along side me for the capillary design and like Jeanna, was a continued source of general and specific knowledge regarding MEMS, research, and fabrication. Tiffany Quy gave assistance with visualization, calibration, and general experimentation. I hope I was as useful training her as Jeanna was to me.

Outside the P^3 team I also received support from WSU staff. Mark Fuller keeps the WSU clean room running and helped me specifically with sputtering and SU8 fabrication issues. His hard work helped make my fabrication a success. Also, the WSU MME machine shop was always supportive of my and many other graduate student's

work. Specifically Henry Ruff and Robert “Kurt” Hutchinson always came through with advice and assistance on various fabrication issues and their service is greatly appreciated. They are model WSU employees demonstrating hard work and a devotion to students.

FABRICATION AND CHARACTERIZATION OF A MICRO CAPILLARY EVAPORATOR FOR MEMS BASED POWER GENERATION

Abstract

Daniel A. Carpenter, M.S.
Washington State University
December 2004

Chair: Robert Richards

A Microelectromechanical System (MEMS) based micro capillary evaporator for power generation was fabricated and characterized. The main goal of this work is to determine the efficiency of an evaporator, where efficiency is defined to be the amount of energy used to evaporate fluid over the amount of energy put into the evaporator. An energy balance on the evaporator is used to determine this efficiency and track where input energy goes.

The evaporator is fabricated on 10mm by 18mm silicon die with a5mm square, 2µm thick membranes at the center. Two concentric, annular platinum Resistance Temperature Detectors (RTDs) surround a platinum resistance heater located in the center of the membrane. A 10mm diameter capillary wicking structure is fabricated over the RTDs and heater on the membrane using an epoxy-based resist, SU8. The SU8 wick pattern, which went through several iterations, consists of structures with 10µm wide channels, with 10µm wide lines and 10µm thick sidewalls.

A series of evaporation experiments are reported. The efficiency of the wicks and the energy balance for the experiments is documented. Both steady state and transient evaporation tests are detailed. During a five-minute period of steady state evaporation the energy into the evaporator is 14.47J. Energy carried away by evaporation is 3.36J.

Energy conducted across the membrane is 15.7J. The corresponding electrical power into the evaporator is 48mW with, 11mW carried away by evaporation, and 52mW conducted across the membrane. Energy dissipated in the evaporator heater minus the energy conducted across the membrane and energy carried by evaporation balance within 27%. RTD1 measured a temperature of 40°C and RTD2 30°C, giving a ΔT of 10°C. The efficiency is 23%.

A transient evaporation test run at 1Hz and 50% duty cycle results in energy carried away by evaporation of 2.51J with energy into the evaporator of 16J over 5 minutes and 13.9J conducted out across the membrane. Energy in minus energy out thus balances within 2%. The electrical power in is 53mW with 8mW of power carried away by evaporation, and 46mW of power conducted out across the membrane. The efficiency of energy of the evaporation in transient operation is 15.66%. RTD1 measured a temperature of 42°C and RTD2 of 22°C, giving a ΔT of 20°C.

TABLE OF CONTENTS

Acknowledgements iii

Abstract v

Table of contents vii

List of figures ix

List of tables xi

Chapter 1 Introduction 1

1.1 Motivation 1

1.2 Background 1

1.3 Research Objectives 9

Chapter 2 Fabrication 10

2.1 Membrane Fabrication 10

2.2 Re-oxidation 10

2.3 Photolithography 11

2.4 Platinum Deposition 13

2.5 Platinum Lift Off 14

2.6 SU8 Wick Fabrication 15

2.7 SU8 Fabrication 17

2.8 Wick Design 1st Generation 19

2.9 Wick Design 2nd Generation 21

2.10 Wick Design 3rd Generation 24

Chapter 3 Experiment 26

3.1 Evaporator Energy Balance 26

3.2 Energy Dissipated in the Electrical Resistance Heater 26

3.3 Energy Conducted Across Membrane ... 27

3.4 RTD Testing Box ... 29

3.5 RTD Calibration ... 29

3.6 Energy Carried by Evaporation ... 31

3.7 Visualization ... 34

3.8 Experimental Uncertainty ... 37

Chapter 4 Procedures ... 40

4.1 Experimental Procedures ... 40

4.2 Steady State and Transient Heat Conduction Experiments ... 41

4.3 Steady state and Transient Evaporation Experiments ... 43

4.4 Visualization Procedures ... 44

Chapter 5 Results/Analysis ... 45

5.1 Steady State Heat Conduction ... 45

5.2 Transient Heat Conduction ... 46

5.3 Steady State Evaporation ... 48

5.4 Transient Evaporation ... 51

5.5 Visualization Results ... 53

5.6 Background Evaporation Corrections ... 54

Chapter 6 Conclusions ... 57

6.1 Conclusions ... 57

Appendix A: SU8 Fabrication Steps ... 59

Appendix B: LabVIEW Procedures ... 60

LIST OF FIGURES

Figure 2-1: Positive Photolithography mask for 5mm 12

Figure 2-2: Photolithography mask for 5mm IGW Oxide 13

Figure 2-3: Platinum Liftoff Process 15

Figure 2-4: SEM Picture of Finished SU8 Wicks, Courtesy J. Martinez 17

Figure 2-5: V Pattern, 1st Generation Wick Mask 21

Figure 2-6: Wedge Pattern, 2nd Generation Wick Mask 22

Figure 2-7: Radial Wick in Wick Pattern, 3rd Generation Wick Mask 23

Figure 2-8: Annular Pattern, 3rd Generation Wick Mask 24

Figure 2-9: Combination Pattern, 3rd Generation Wick Mask 25

Figure 3-1: Power In Test Circuit 27

Figure 3-2: 5mm Heater/Dual RTD 28

Figure 3-3: RTD Calibration Curve 966I 30

Figure 3-4: Evaporation Experiment Schematic 33

Figure 3-5: Visualization Setup 35

Figure 4-1: Assembled Carrier 41

Figure 4-2: Schematic of TTL Circuit, Courtesy S. Whalen[35] 42

Figure 5-1: Steady State Heat Flux 5,7,9 Volts 46

Figure 5-2: Transient Heat Flux 7 Volts 47

Figure 5-3: Steady State Evaporation 6 Volts 48

Figure 5-4: Zero Power Evaporation 49

Figure 5-5: Transient Evaporation 10 Volts 51

Figure 5-6: PIV Visualization 6.7 Volts 966I 53

Figure 5-7: Zero Power FC77 Evaporation 55

Figure 5-8: Steady State FC77 Evaporation 7 Volts.. 56

Figure B-1: LabVIEW Front Panel – Analog Out For TTL 61

Figure B-2: LabVIEW Front Panel – Analog Input.. 62

LIST OF TABLES

Table 2-1: Wick Dimensions 1st Generation Mask 20

Table 5-1: Evaporation Summary 58

Table 5-2: Energy Balance Summary 60

CHAPTER 1 INTRODUCTION

1.1 Motivation

Microelectromechanical systems (MEMS) are proving their usefulness in technology today. Both in terms of research and commercial applications, the MEMS field has been predicted to parallel the rapid growth of the computer industry.[1] Having shared many of the same fabrication roots, the similarities between these two technologies are not difficult to see. MEMS have taken hold of such niche applications as accelerometers for automobile airbags, absolute pressure sensors for engines, inkjet printer heads, and read/write magnetic heads for hard drives.[2] Although these specific markets have proven to be very lucrative, MEMS devices can also help with many other widespread challenges.

1.2 Background

Thermal management is an increasingly difficult engineering problem. Industry widely uses thermal control; examples range from the radiator in an automobile engine to cooling microchips. Heat dissipation in microprocessors is becoming the challenge of the computer industry. Chip power dissipation levels are currently at 10-50 W/cm^2 and levels of 100 W/cm^2 are predicted for the future.[3,4] Previously, as heat loads of chips approached the failure temperatures of the substrate, finned metallic heat sinks mounted directly on the processor provided adequate cooling.[5] The heat load increased as the number of transistors in each chip increased to meet the demands of faster processing. Unfortunately, current fan heat sink combinations cannot keep up with the projected heat load.[6] This problem will severely limit the further development of the computer chip if not properly addressed.

Along with the fans and heat sinks, much research is now going into spray cooling.[7] This thermal solution involves a small pump that sprays a continuous jet of liquid droplets directly onto the processor. The heat dissipation of such units can be 1200 W/cm^2. Some of the drawbacks of theses systems are their size, complexity, and power draw that they add to the overall system.

Many researchers, however, are taking a different approach. Instead of bulky pumping devices, micro grooves and heat pipes that rely on capillary pressure and evaporation are being fabricated directly into silicon substrates. These offer relatively high heat transfer rates 700 W/cm^2, simplicity in design, and low cost.[8,9]

Evaporation of thin films provides an effective mechanism for cooling and heat transfer because of the phase change of the fluid.[10] Evaporation of thin liquid films carries large amounts of energy. The effectiveness of latent heat transfer provides the motivation behind both micro grooves and micro heat pipes used to cool computer chips. Phase change can also be used effectively in microscale actuators and engines. One such example is the P^3 micro heat engine under development at Washington State University. This engine is based in a cavity bounded on the top and bottom by silicon membranes. The top membrane is covered with a piezoelectric material (PZT) and gives off a charge when mechanically deformed. The bottom membrane acts as an evaporator. The cavity between the two membranes contains the working fluid PF5060DL, a fluorinated refrigerant made by 3M. When heat is added to the evaporator on the bottom membrane, the refrigerant vaporizes. The vapor expands against the upper membrane, stretching it and doing work. This stretching of the membrane causes the PZT to strain and produce a voltage potential. The heat transfer into the device is a crucial part of the process. If the

heat input is not used efficiently to vaporize the working fluid, the efficiency of the device suffers. As a result, using the heat input efficiently during evaporation is important to the success of the engine. Characterization of the heat addition process is also essential towards increasing the efficiency of the device. For these reasons, much effort has gone into understanding where energy goes during the heat addition and evaporation process, and how to control these heat fluxes.

A primary requirement of evaporation heat transfer is that the fluid be kept in close contact with the heat source. Through capillary pressure, a micro groove can "pump" fluid from a reservoir to a heat source as the fluid is evaporated. This ensures a continuous amount of fluid being delivered to the heat source and therefore continuous cooling by evaporation. The capillaries also control the thickness of the film of fluid as it is pulled down the channel. Often these grooves are etched into the silicon substrate itself, usually in a "v" formation to give the acute angles necessary for capillary pressure differences. These grooves can be oriented in a variety of patterns but basically serve the same purpose of moving fluid into contact with a heat source in need of cooling.

A slightly more complicated micro cooling device, the micro heat pipe (MHP) employs the use of micro grooves but adds a return mechanism for the evaporated gas. With this in mind, the heat pipe uses the same general idea of the groove but has a sealed top and cycles the evaporated fluid from the evaporator back to a condenser, where it can reject its heat upon condensation and then be returned to the evaporator via the groove structure. Macro scale heat pipes employ a wicking structure to move the fluid but on the micro scale, the geometry of the grooves themselves provide the wicking power.[11] There has been extensive research into each of these devices, their behavior, and their

applications, some of which will be examined in the following. They are beneficial because of their improvement of the heat transfer process overall but also because they allow the evaporation process to be controlled and studied. This leads to a greater overall understanding and ultimately a better device.

The micro groove solution to cool electronics has become popular in the last decade.[8] Research in micro grooves has focused on a myriad of different topics many of them concentrating on heat transfer[12] both transiently[13] and steady state,[14] maximum heat transport capacity,[15,16,17] and flow boiling.[18,19] The individual components of the fluid flow inside the channel have been studied including the meniscus[20,21] and thin film.[22] Many different approaches to applying these grooves to cooling have also been investigated [4,9,11,23,24] and almost all research explores different ways to fabricate the device. These different aspects all lead to a greater understanding of the MHP and its ability to control heat.

Research into the dynamics of the main component, the micro groove, is one of the first steps toward a complete characterization of the MHP. Once the mechanisms that affect groove design are understood, investigation of the MHP overall is possible. The two primary goals of micro groove research are to get the maximum heat transfer and predict the groove design that will give the best capillary performance. These two are closely related. Peterson *et al.* explains the relationship between capillary performance and heat transfer by focusing on the meniscus formed when the fluid comes into contact with the groove wall.[22] The region connecting the evaporating thin film region and adsorbed layer, the thinnest region, is where the majority of heat transfer occurs. This is caused by how thin the film gets. When heat is added to the groove, the meniscus

recedes axially along the groove length, thinning the film. The capillary pumping, or wicking action, of these grooves is a result of the film receding into the groove.[22] Changing the number, length, and shape of the groove will vary these properties.

On the micro scale heat pipes are long (1micron to 20 mm)[25] narrow tubes in direct contact with a heat source. The end of the MHP in contact with the heat source is referred to as the evaporator and the heat rejection end is called the condenser. The fluid is boiled and evaporated off the evaporator, taking heat from the hot spot and rejecting it at the condenser. The cooler temperatures here allow the gas to condense back to a liquid. As mentioned earlier, capillary pressure often facilitated through a wick on the macro scale, continually "pumps" fluid from the condenser to the evaporator. On the micro scale, the heat pipe relies on the geometry to cause capillary forces to pump the fluid.[26]

Usually heat pipe geometry is dictated by ease and availability of fabrication equipment but different groove shapes have been examined for overall performance.[11,25,26,27] These grooves were triangular, trapezoidal, and rectangular and had dimensions on both the meso and micro scales. It is important to point out the differences in measuring performance of micro grooves and heat pipes. Usually either heat flux or thermal conductivity is used to measure improvements in thermal management. Thermal conductivity has units of W/mK and improvements are usually compared to the thermal conductivity of silicon. High conductivity materials such as polycrystalline diamond have a thermal conductivity of about 1200 W/mK.[25] Heat flux, on the other hand, is measured as power over area and is usually expressed in units of W/cm^2.[28]

R Hopkins *et al*[27] examined performance of varying groove geometries with respect to max heat flow rate and heat flux for a range of operating temperatures, orientations, and heating configurations. The heat pipes examined were relatively large; the rectangular grooves were 0.20mm by 0.42mm. Sixty-two of these grooves were machined in a side-by-side orientation. The max heat load was found by measuring temperatures at different heat loads, 60 – 95 °C, until dry out of the evaporator was observed. The maximum heat flux on the evaporator wall was found to be 90 W/cm^2 in horizontal orientation and 150 W/cm^2 in the vertical orientation.[27]

Orientation of MHPs also affects their overall performance and use. To maximize real estate in the very small environment of the microchip, designers have arrayed the micro grooves in different patterns to help maximize cooling and decrease hot spots. One of the larger micro heat pipe arrays was fabricated by Ponnappan[11] and uses 6.35mm by 12.7mm standard refrigeration copper tubing. This approach is unique because of the larger size and the addition of a wick made of copper mesh screen cloth. These miniature heat pipes with added wick gave a 115 W/cm^2 heat flux. They were tested at 90 °C operating temperature and horizontal orientation and are very comparable to the performance of the wicks by Hopkins.[27]

Le Berre *et al*[25] experimented with the effects of differing geometries, working fluids, and adding an extra artery below the heat pipe groove for fluid transport. Two heat pipe arrays were fabricated in silicon, one with 230 micron wide, 170 micron deep channels and the other with 500 micron wide, 340 micron deep channels. Both were triangular and were formed using anisotropic etching of silicon. The second array design (500 micron wide) had v grooves etched in a separate wafer that was bonded

underneath the wafer containing the heat pipes. These separate grooves were used to return the fluid to the evaporator. This design increases the cross sectional area for fluid transport and limits the interfacial friction between liquid and vapor.[25] For heat pipes cooling temperatures below 125 °C, methanol and ethanol were used as the working fluids because of their thermophysical characteristics. These are the most common working fluids along with water, FC 72, and acetone.[26] The results for the standard triangle groove (no liquid arteries) with a heat input of 0.5 to 4 watts showed little improvement in terms of thermal conductivity. The array of heat pipes with the triangular arteries below however, had a 300% improvement in thermal conductivity when compared to silicon.

Peterson *et al* fabricated micro grooves as small as 45μm diameter to study their effectiveness at cooling a heated wafer.[26] He used two different fabrication methods and wafer geometries. First, the above mentioned 45 micron wide by 80 micron deep rectangular grooves were fabricated using a silicon dicing saw. The second array of triangular 120 micron wide by 80 micron deep grooves was fabricated in a silicon wafer using a KOH etch. Using methanol as the working fluid with an input power of 4 watts, Peterson found that the max chip temperature was reduced by 14.1 °C and 24.9 °C for the triangular and rectangular grooves, respectively. The effective thermal conductivity was increased by 31% and 81%.[26] This is noteworthy because of his exploration and comparison of different channel shapes as well as the scale he used, less than 100 microns for channel width.

Design of both the evaporator and condenser also affects the overall performance of the MHP. The condenser is usually coupled to a heat sink to maintain a

constant temperature while the evaporator is in contact with the heat source. The geometry of the two ends of the heat pipe has been found to affect the overall thermal resistance. Hopkins defines thermal resistance as the overall end cap to end cap temperature drop divided by the total applied heat load.[27] At low temperatures the thermal resistance is high since the fluid is in a relatively thick film. The resistance decreases as temperature is increased but it is also affected by the size of the evaporator and condenser. The larger the surface area the thinner the film and hence better evaporation.

Along with the environmental and performance constraints, fabrication constraints pose many of the design limits on micro heat pipes. Many heat pipes are formed in triangular configurations using orientation dependent etching such as KOH.[26,27] This gives the sharp angle needed to wick the fluid and is easily manufactured using current micro fabrication techniques. It is highly controllable and offers very fine resolution features, often as high as 1 micron. The other common groove shape is axial rectangles. These are usually fabricated using very fine silicon dicing saws.[26] This is a viable option if wet etching is not easily used or if rectangular channels are desired over triangular ones but leaves slightly rounded corners and residue in the channel from the machining process. In order to complete the MHP and not just leave open grooves, a cover must be sealed over the micro channels. Another silicon wafer is a simple solution and can be hermetically sealed onto the top of the wafer with the MHPs.[25] If the flow inside the channels is to be visualized; silicon will not work because it is opaque. Instead, Pyrex glass can be bonded to the wafer using ultraviolet light and optical adhesive.[26] This yields a sealed yet visible grooved MHP. This is often a key process for

the characterization since it gives insight into the performance and operation of the evaporator.

Pulling this into perspective, Benson *et al* fabricated MHPs into a multi chip module (MCM) made of silicon. A pattern of wicks in the shape of long armed crosses is plasma etched into a silicon wafer and then bonded to glass. The result is a 5 factor improvement in heat spreading capability over a standard silicon MCM. This is comparable to the performance of a polycrystalline diamond substrate yet remains at the low cost of silicon.[9]

1.3 Research Objectives

The research objectives of this project are first, to fabricate a micro groove wicking structure to control fluid contact with the heat source in the evaporator, and second to characterize the efficiency of the evaporator. Part one, fabrication of the wicking structure, is accomplished using an epoxy-based resist that can be patterned through standard photolithography processes. The wicks are patterned on top of a silicon membrane with a platinum resistance heater and two RTDs. Part two, characterization of the evaporator efficiency is accomplished through an evaporation experiment and energy balance. A very accurate digital scale is used to measure evaporation mass flow rates. Two concentric annular RTDs are used to measure conductive heat transfer along the membrane evaporator. A long distance microscope and digital camera is used to visualize the flow inside the channels.

CHAPTER 2 FABRICATION

2.1 *Membrane Fabrication*

Integral to operation of the P^3 micro heat engine is the membrane design. In order to combine multiple engines together, both the top (generator) and bottom (heater) are constructed on thin silicon membranes. Olson outlines the detailed fabrication procedures for membranes.[29] The process involves etching the membranes into a silicon wafer. First, one side of the wafer is doped with boron to act as an etch stop. The thickness of the boron layer determines the thickness of the membrane. Next, a low temperature oxide (LTO) layer is grown on the wafer and then patterned to give the desired arrangement of membranes. An anisotropic etchant, ethylene diamine pyrocatecol (EDP), is then used to etch all of the silicon not covered by the etch mask down to the boron layer. EDP is very anisotropic and works well because of its affinity for the (001) plane of silicon. As a result it etches down much faster in the 001 plane than other directions and results in a pyramidal shaped pit. Since the etch does not go vertically down, special care must be taken into designing the oxide etch mask. Upon etching, the wafer is patterned with square membranes and is ready to move to the next fabrication process, re-oxidation.

2.2 *Re-oxidation*

After membranes are fabricated, a new oxide layer is grown over the entire wafer. This is the same wet oxide process used for the LTO but is run for a shorter time to achieve a 100 nanometer thick oxide.[30] This extra oxide is added to give electrical insulation between the electrodes and boron layer of the silicon. Without this layer,

electrical shorts are more likely to occur, making many devices such as RTDs and heaters unusable.

2.3 Photolithography

Photolithography is used to pattern the platinum RTD. Platinum is not easily etched at WSU and requires photolithography before sputtering to allow the unwanted platinum to be lifted off the wafer. Photolithography takes advantage of the properties of certain polymers called photoresist. These polymers, when exposed to ultraviolet light, change their material properties by increased cross-linking. In the case of a negative lithography process, the part of the material that is exposed to UV light undergoes heavy cross linking and when later immersed in a developer solution, is not washed away like the unexposed resist. A black and clear photomask is placed between the light source and substrate to give the photoresist coating the desired pattern after development.

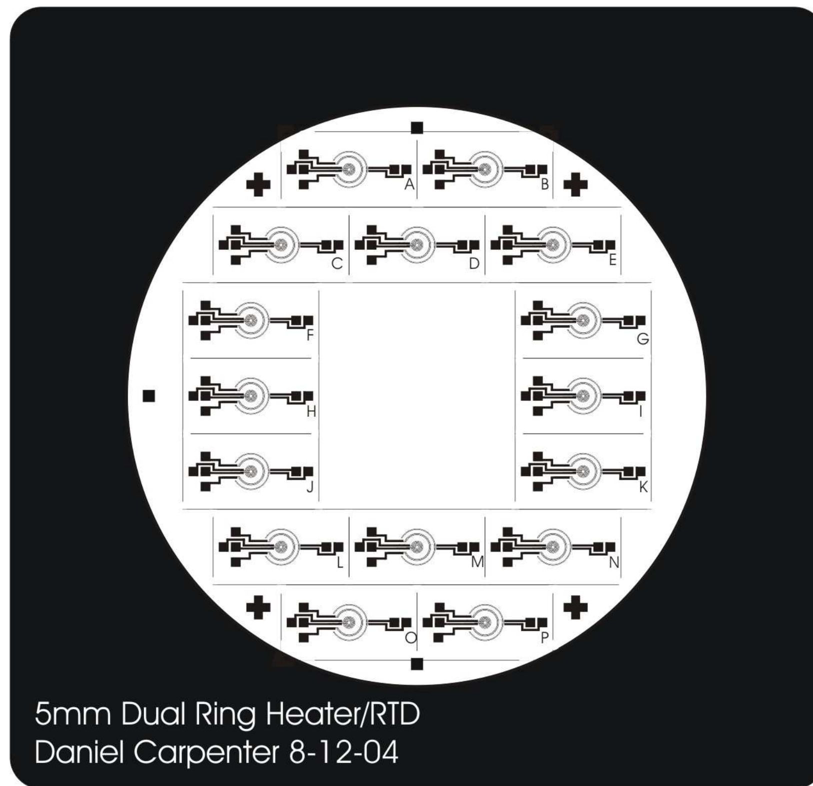

Figure 2-1: Positive Photolithography mask for 5mm

The wafer is then exposed to UV light through the mask, changing the material properties of the portion of the resist that is uncovered. There are a few things to note about the heater mask shown in Figure 2-1. It is composed of the standard pattern of 16 individual die arrayed around a circle and has the three small squares and large rectangle to align with the oxide mask. This ensures that the RTD and heater are centered perfectly on the membrane. The four plus signs in the four corners of the pattern are used to align the wick mask with the heater mask, ensuring that the wicks, like the heaters, are at the exact center of the membranes.

Any fabrication process using photolithography requires the use of a photomask. Figure 2-2 shows the oxide mask for a 5mm membrane wafer. This mask is used to pattern the oxide layer prior to EDP etching.

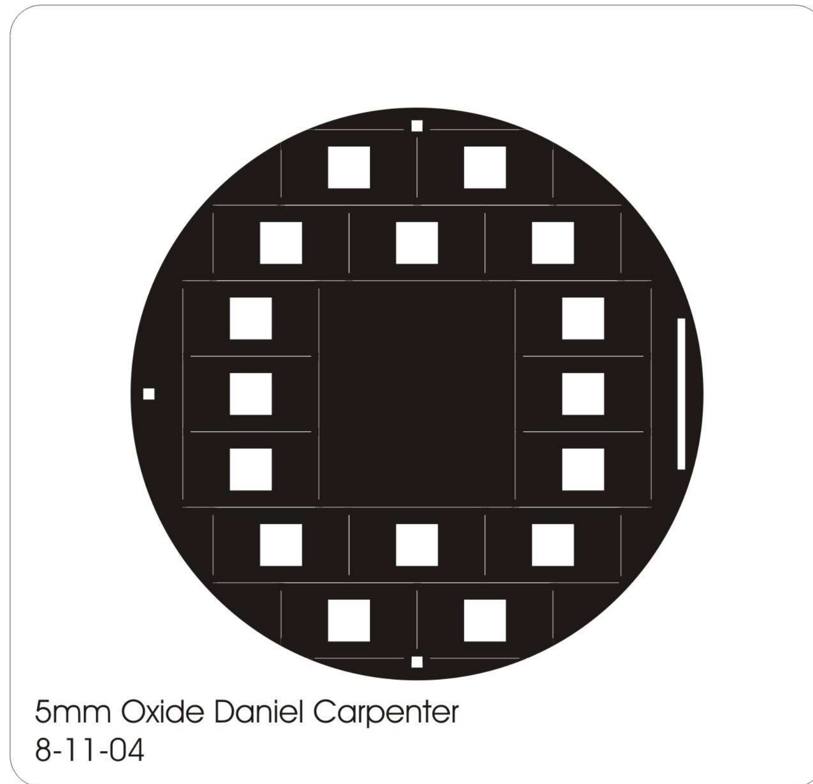

Figure 2-2: Photolithography mask for 5mm IGW Oxide

The 16 squares arrayed around the wafer will become the membranes. Each membrane has a 10mm by 18mm rectangle around it, defined by thin lines. These lines are for dicing of the wafer later and will allow the wafer to be broken into 16 individual pieces, in this case, 16 heater die will come from this wafer. The center of the wafer is left empty because a vacuum chuck is used to hold the wafer during spin coating and any membranes there would break. The long rectangle on the right side and the three small squares on the top, bottom, and left side are used as alignment marks for further patterns.

2.4 Platinum Deposition

Previously, the P^3 has used gold as the material for the resistance heater.[29] Gold is sputtered onto the bare wafer and then patterned into a ring design using photolithography. Olsen and Olsen describe the sputtering process in detail including

instructions and proper time to thickness ratios for both gold and platinum.[29,30] Magnetron sputtering uses ion bombardment to remove material from a target and deposit it on the substrate.

For the case of RTDs, platinum is considered the standard in reliable temperature measurements.[31] Because of this, the two RTDs on the membrane that make the energy balance possible are fabricated from platinum. In order to simplify the process and not sputter and mask multiple times, the heater when combined with the dual RTDs is also made from platinum.

2.5 Platinum Lift Off

The patterned photoresist on the wafer acts as a sacrificial layer and allows the removal of the unwanted platinum. After the silicon oxide has been covered with resist and patterned into the heater/RTD design, platinum is then sputtered over the entire wafer. Titanium is used as an adhesion layer between the silicon oxide and the platinum. Next, the platinum covered wafer is immersed in acetone until the unwanted platinum is “lifted off” and only the desired heater/RTD pattern remains. This is possible because the platinum is sputtered over a partially resist covered wafer. The outcome is depicted in Figure 2-3 and results in a stair step like effect and leaves parts of the resist exposed. The exposed resist is then dissolved by the acetone, taking away the platinum that was on top of it. Detailed fabrication steps for platinum liftoff were developed by Cho.[32]

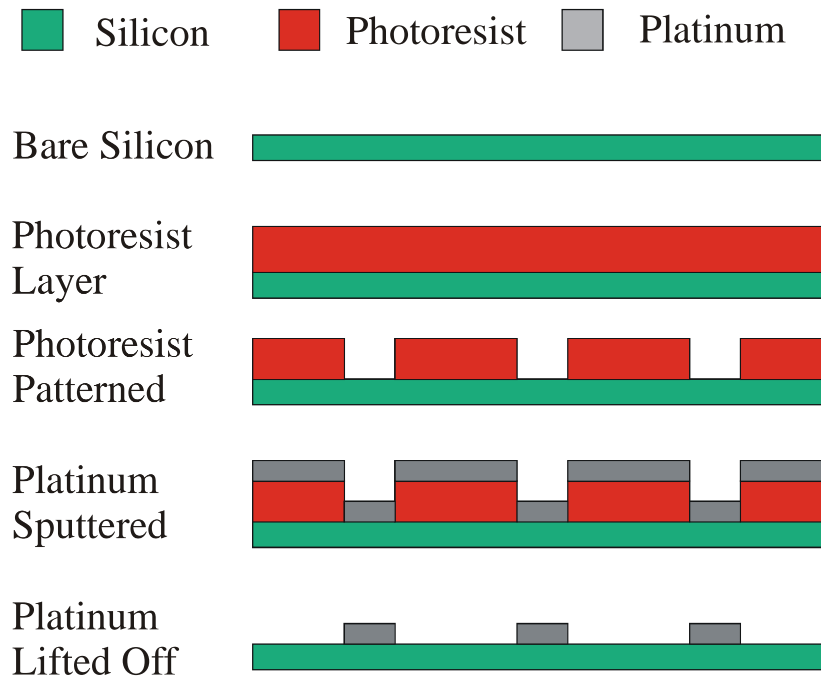

Figure 2-3: Platinum Liftoff Process

2.6 *SU8 Wick Fabrication*

SU8 is an epoxy based resist that was first developed by IBM in 1989 specifically for high aspect ratio MEMS applications.[33] The key to SU8 success is its very low absorption in the UV spectrum. This allows very thick coatings to be processed in one exposure with sharp features and aspect ratios as high as 20:1.[33,34] It reacts with ultraviolet light and can be patterned through standard photolithographic techniques. Unlike AZ5214 resist, however, 2010 SU8 uses a negative process. With this, the SU8 that is exposed to UV light is what remains and the unexposed is dissolved away. SU8 is used to fabricate a micro grooved wicking structure on top of the membrane and platinum RTDs. The wicks require 10μm thick sidewalls to give a sufficient rate of evaporation.[35] These channels are also required to have straight, vertical walls both to give the acute angles needed for wicking, and to give clean channels that would not impede liquid flow.

Since these wicks are fabricated on top of a platinum resistance heater, they also need to tolerate the high temperatures encountered during the heat addition process in the engine. Although there are several thick photoresists that can be spun to 10 microns, high aspect ratio structures are difficult to obtain. The thick photoresist is also unable to withstand the high temperatures during heat addition. Several melted during evaporation tests. In contrast, SU8 excelled at giving vertical sidewalls, is relatively easy to fabricate, and demonstrates adequate heat tolerances. These aspects along with the plethora of available information on its processing and characteristics,[36,37,38,39,40] makes SU8 a good choice for fabricating the micro wicking structures. Procedures for SU8 fabrication are in Appendix A and an SEM picture of a finished wick is shown in Figure 2-4.

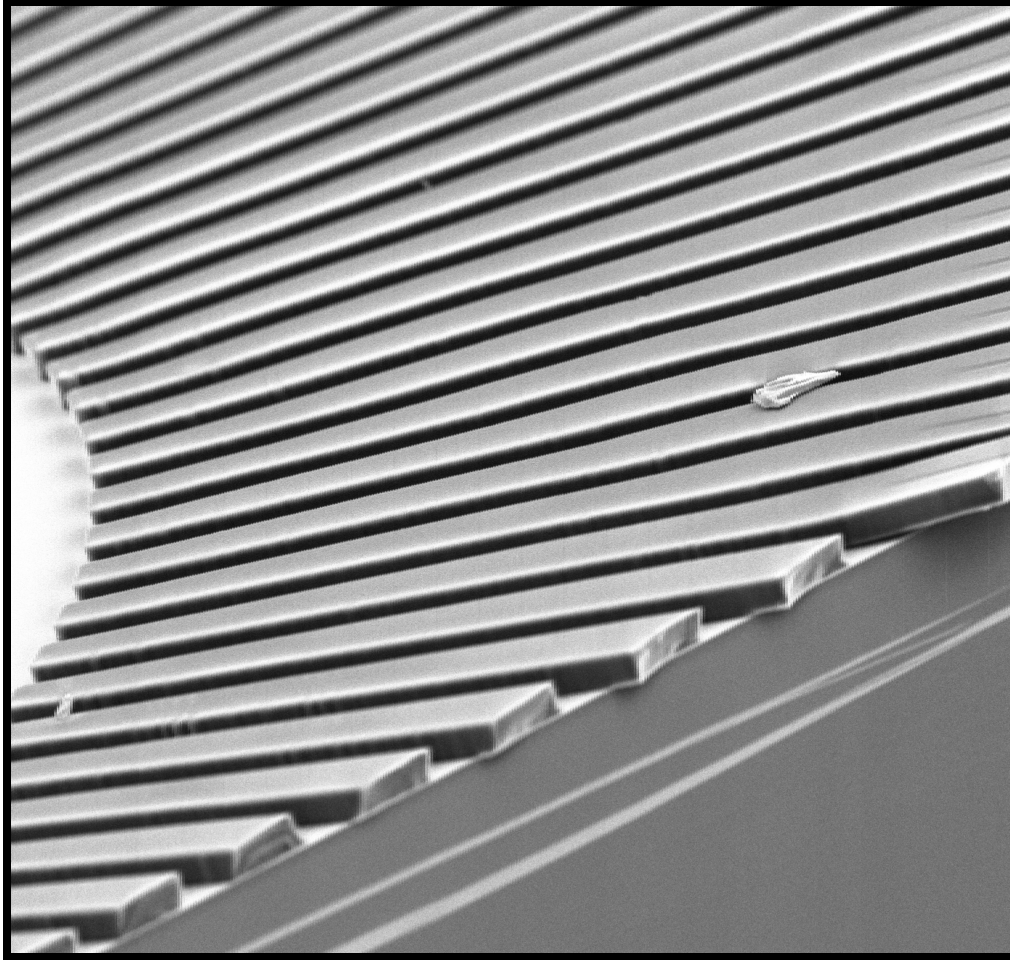

Figure 2-4: SEM Picture of Finished SU8 Wicks, Courtesy J. Martinez

2.7 SU8 Fabrication

Exposure and spin times for the SU8 were determined empirically. MicroChem publishes guidelines, these guidelines vary with application parameters such as exposure equipment, substrate, spin coating, and heating. To determine exposure times for this application, an exposure matrix was constructed using a single sided silicon wafer, the chrome plated wick mask, and an aluminum foil "picture frame" mask. The "picture frame" mask was a sheet of aluminum foil with a small square, the size of a wick pattern, cut away to allow light to penetrate. This mask was then placed between the ultraviolet light source and the chrome and glass mask. The single sided wafer was then coated with

SU8 and instead of one exposure for the whole wafer, the aluminum foil mask was used to test several different exposure times on the same wafer by exposing, moving the mask to another spot, and exposing again until the whole wafer had been used. Fabrication was then finished using the standard processing and the results were checked under a microscope. A large spread of exposure times were used, from as short as 5 seconds, to as long as 1.5 minutes. The goal was very steep, high aspect ratio sidewalls. An exposure time that was too long gave pyramidal features with sloping walls instead of vertical. A too short exposure time gave "t topped" features that had significant undercutting below the surface of the SU8. This process was repeated with several iterations, each time narrowing the exposure times down until 18 seconds was found to be the ideal time for a gold and silicon oxide substrate. When the heater and RTD design were later changed to platinum, the exposure matrix was again employed because the reflectivity change from platinum to gold was enough to affect the SU8 development. The platinum and silicon oxide substrate was found to have a 24 second exposure time. This method must be used any time there is a change in either substrate or pattern, since each of these can make the previous exposure time unusable.

An optimum spin speed was also determined empirically. The same test wafers that were used for exposure were also used to test various film thicknesses and spin speeds. After processing, profilometry was used to measure the height of the pattern. 2000 rpm was found to give a sidewall height of between 8 and 10 microns and was used as the standard spin speed for SU8 wick fabrication.

During the continual testing for proper exposure time, surface cracking became a recurring problem. The cracks were thin and seemed to appear at random throughout the

SU8. An increase in both post exposure bake (PEB) times of one minute seemed to alleviate the problem. MicroChem's processes instructions called for a 1 minute PEB at 65 °C followed by 2 minutes at 95 °C. The extra minute was added to each of these steps. Also, a cooling step was introduced between post exposure and development to avoid cracking caused by rapid temperature decrease upon immersion in developer.

Adhesion was occasionally a problem throughout processing. The 5 micron features of the first generation mask often would wash away in the IPA rinse and canned air steps after development. If alignment was a problem and the wicks didn't have very much length after the gold heater, the ends would often peel back or be pushed to the side. Variations in any of the other fabrication processes seemed to adversely affect adhesion as well. If the exposure time was too short or the bake times/temperatures insufficient, the fine wick features would lift off the wafer during development. Problems with the oxide layer or platinum were also thought to contribute to poor adhesion.

2.8 Wick Design 1st Generation

As mentioned in the literature review, there are a myriad of different factors that affect the overall wick performance. The primary function of the wicks during evaporation is to keep fluid in contact with the heat source. Several variations on a simple radial design of straight channels are considered here. The dimensions of these structures are limited by fabrication constraints. The most important constraint is that photolithography in our clean room is limited to approximately 5 micron features. A 10 micron wide channel has been found to be usable and within limits of fabrication. Because wicking is best in a wick channel of one to one ratio, the desired thickness of the

channel is also 10 microns. A line thickness of 15µm gives a wider contact area and improves adhesion. Once the channel width and line width are selected, the remainder of the design is determined by the number of lines that can be combined around the membrane without interfering with each other. Since the P^3 engine is run with several different membrane sizes, first generation wick mask designs are based on several different radial wick designs, all centered radially on a membrane. These are listed in Table 2-1.

Membrane Size	2mm	3mm	4mm	5mm
Number of wicks	122	400	350	450
Line length	300µm	200µm	200µm	200µm
Line width	15µm	5µm	15µm	15µm
Gap	10µm	10µm	10µm	10µm

Table 2-1: Wick Dimension 1st Generation Mask

Each pattern stretches only to the edge of the membrane and is trimmed to a square to match the membrane edges. For the 2mm pattern, the wicks lines are trimmed at the inside point where they intersected each other, making a "v" shape. Unfortunately, this v-shape causes a stress concentration at the "v" causing the wick lines to pull towards each other.

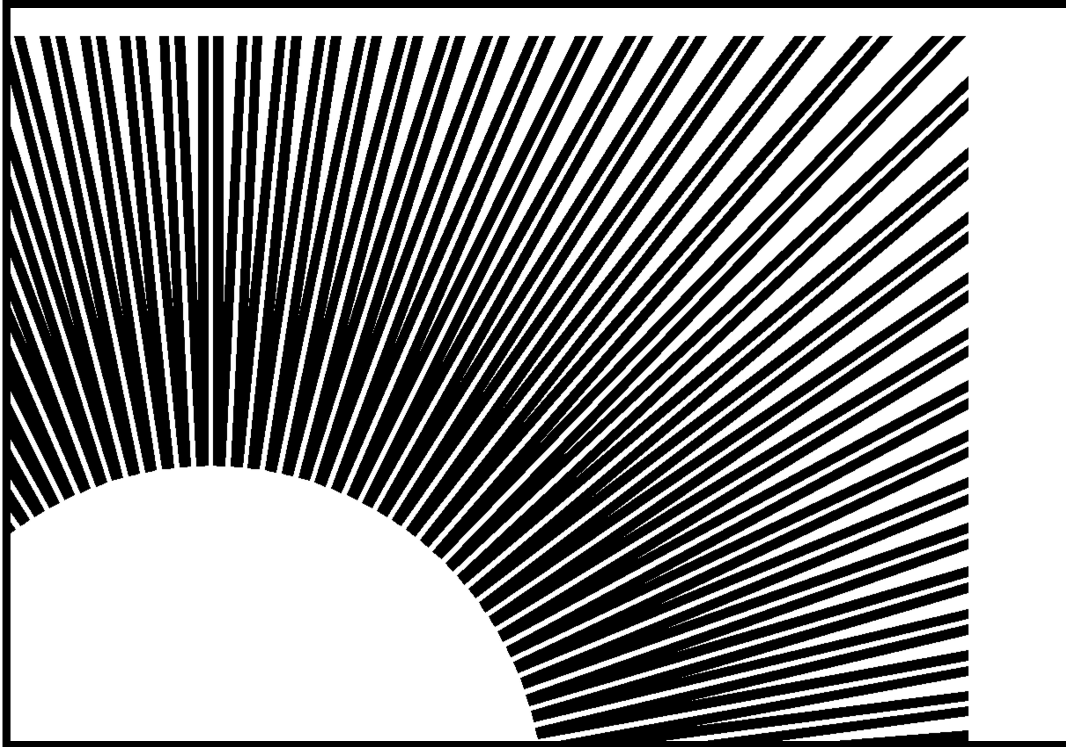

Figure 2-5: V Pattern, 1st Generation Wick Mask

Other patterns look much the same but eliminate the problematic "v" by having sufficient space that the lines do not intersected. Figure 2-5 shows a depiction of one photomask pattern used for SU8 wick fabrication. Since SU8 is a negative process, the part that is exposed will remain after development. This means the desired wick pattern would be transparent on the mask, depicted by the black areas in Figure 2-5, and the rest would be opaque chrome, depicted by the white area.

2.9 Wick Design 2nd Generation

It is essential for the wicks to reach to the edge of the 10mm die to allow the fluid to wick from the fluid reservoir. With that in mind, the first two constraints for the second generation of wicks are (1) channels that go to the edge of the die and (2) channels that do not interfere with each other. A long wedge of SU8 fits these design criteria and alleviates the need for the troublesome "v" intersection in the previous

design. The wedge is very wide at the outside edge and tapers to a narrow width at the inside of the pattern. A series of wedges are arrayed in a circular pattern spaced at 10 micron gaps apart from each other as shown in Figure 2-6.

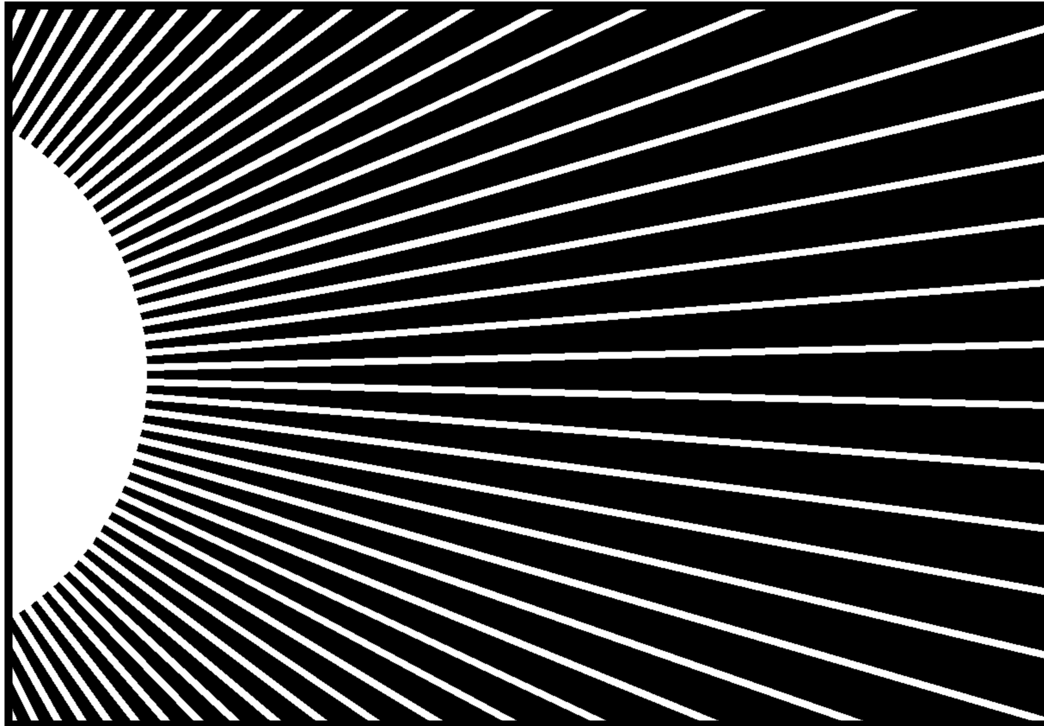

Figure 2-6: Wedge Pattern, 2nd Generation Wick Mask

The SU8 is fabricated into the tapering “wedges.” The constant width gaps between them form the empty wick channels used to move the fluid.

Ideally, the wick design would have as many channels as possible to allow for the greatest amount of fluid evaporation. Figure 2-6 shows that the limitation to the number of channels for this design is the inside circle diameter. The wicks eventually run into each other and constrain the total amount of possible channels. A design that increases the area of the channels consists of a constant thickness SU8 wall separating tapering channel gaps. Such a design increases the amount of fluid to wick between lines. However, this design accomplishes this goal at the cost of the 1 to 1 aspect ratio provided

by the constant 10 micron gap. To offset this wick aspect ratio problem, patterns of additional lines can be added between channels to give additional capillary pumping surface and to keep the aspect ratio close to 1 to 1. This design is depicted in Figure 2-7.

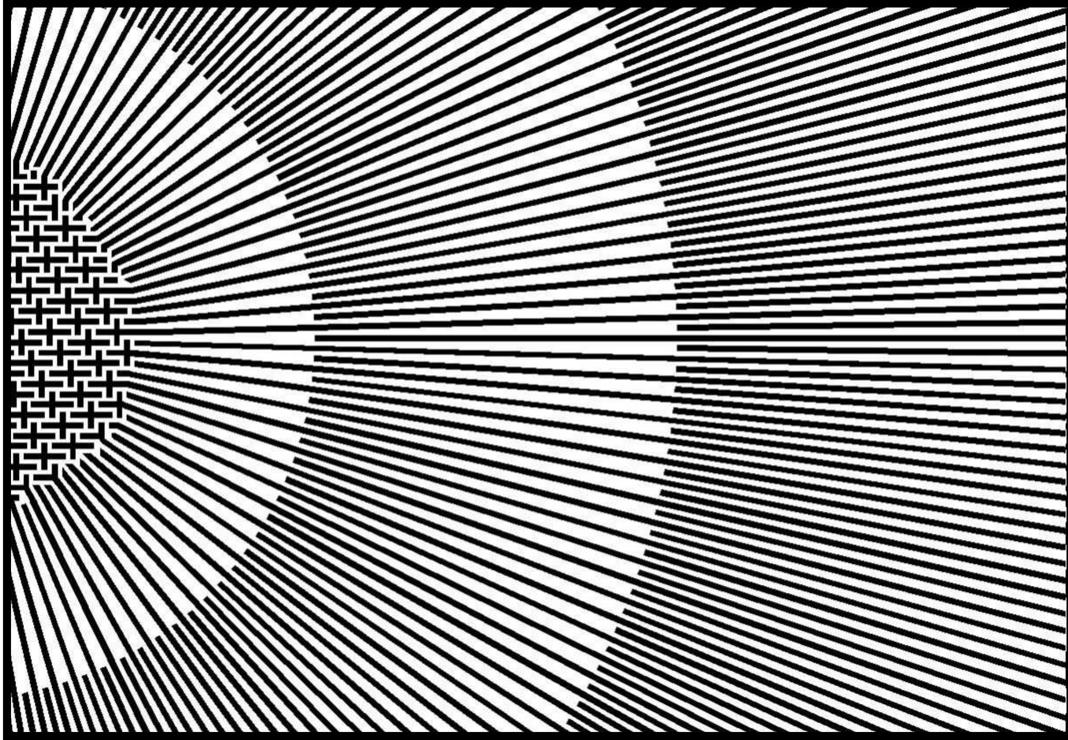

Figure 2-7: Radial Wick in Wick Pattern, 3rd Generation Wick Mask

The constant width black lines in this picture are the SU8 wicks and the tapering white space between is the gap for the fluid to flow. When the gap becomes significantly large because of the taper, more lines are added to the array. The wick lines cannot be extended further into the center circle or they will run into each other and seal off the channels. For this reason, an array of plus signs with long side arms was attached to the end of the wick lines in an attempt to give some pumping power all the way to the very center of the pattern.

2.10 Wick Design 3rd Generation

A third generation wick mask was made to further increase the amount of fluid available for evaporation. The channels converging at the center of the wick restricted the number of possible channels in both previous wick patterns. An annular pattern can overcome this problem. Concentric channels can be defined to the center of the membrane, giving a very high amount of surface area to be filled with fluid. This wick pattern is composed of annular channels that fill from a radial artery fed by two separate fill holes on opposite sides of the membrane as depicted in Figure 2-8.

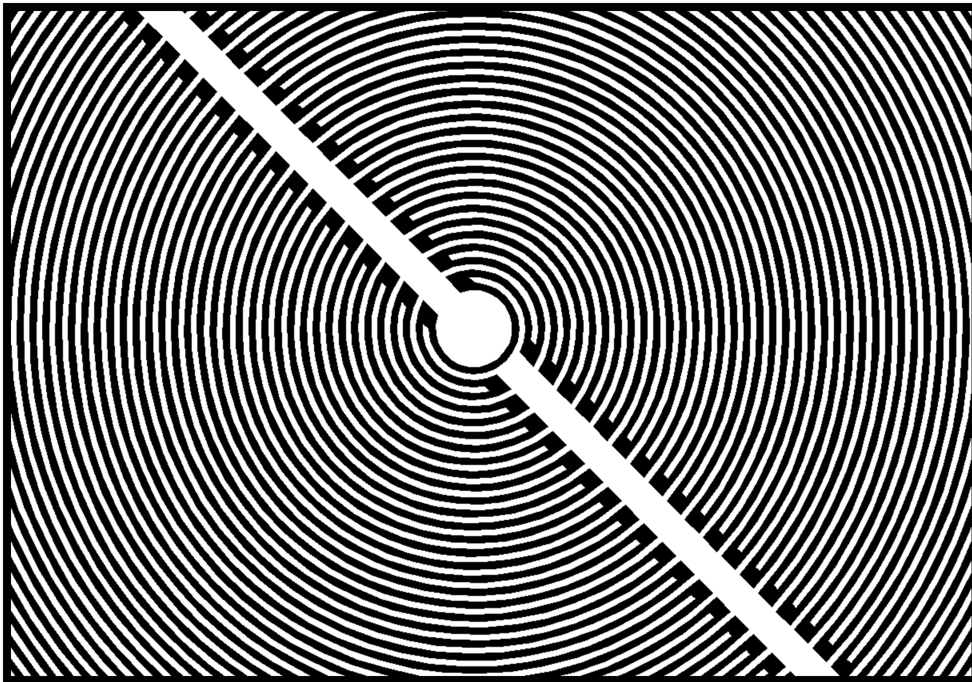

Figure 2-8: Annular Pattern, 3rd Generation Wick Mask

This design gives the largest amount of fluid to evaporate. However, because of the great length of the channels, the wick requires a large amount of time to fill. To overcome the limitation of filling speed, a combination of the radial and annular wicks is defined on the same mask in an attempt to get the best of both fill rates and total amount of membrane coverage. It is composed of radial lines arrayed around the center of the membrane with

annular circles overlaid to form a straight line, annular combination as shown in Figure 2-9.

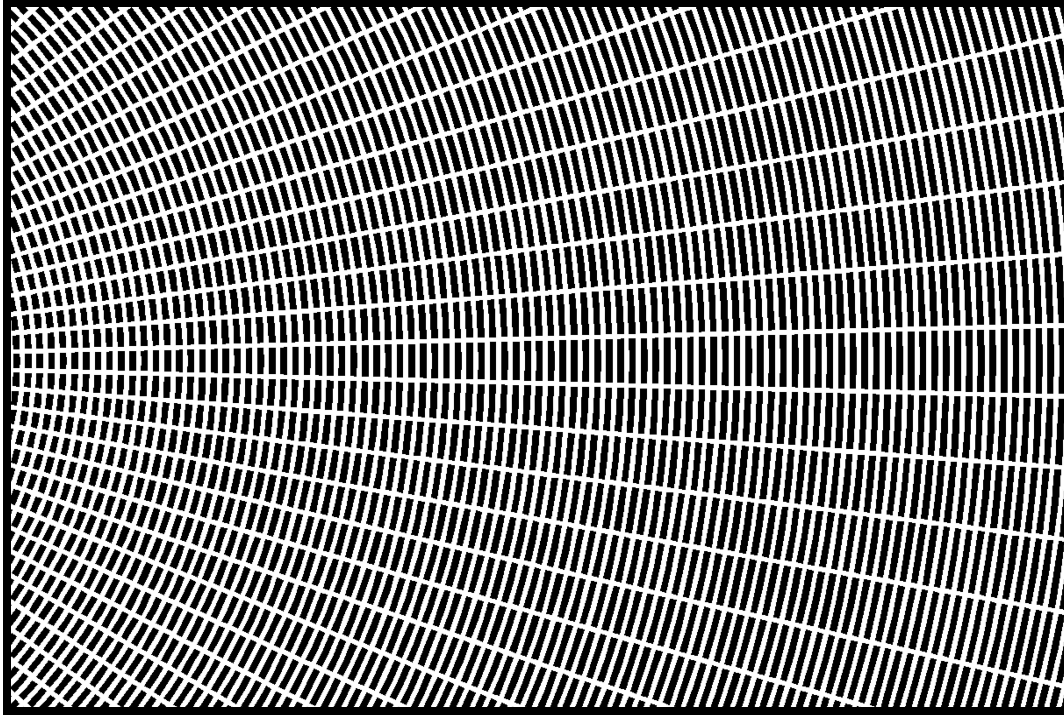

Figure 2-9: Combination Pattern, 3rd Generation Wick Mask

The third generation mask is composed of 5 radial wick patterns, 5 annular wick patterns, and 6 combination wick patterns. All of these masks have features that are well below the printing limits at WSU. As a result, the designs were drawn in AutoCAD and the masks patterned in chrome on a soda lime or quartz substrate by Photo Sciences Co. The result is a clear mask with a negative pattern of chrome having the exact feature of the AutoCAD drawing.

CHAPTER 3 EXPERIMENT

3.1 Evaporator Energy Balance

The goal of these experiments is to measure the efficiency of a wicking evaporator. Efficiency is defined as desired output over required input.[41] The efficiency is therefore the energy carried away by latent heat of evaporation over thermal energy added to the system. To give a complete picture of the evaporative heat transfer process, an energy balance on the evaporator is determined.

Two experiments, (1) a conductive heat flux and (2) an evaporation experiment are used to characterize the energy flows. During these experiments, there are three areas where the energy must be tracked to give a complete understanding of the evaporator. First, the energy going into the system as electrical energy dissipated in the resistance heater must be measured. Second, the energy that travels across the membrane as conductive heat flux must be measured. Third, any energy that is carried away by evaporating the working fluid must be measured. These three energy terms are summed together to give a complete picture of where energy goes and how efficiently it is used.

3.2 Energy Dissipated in the Electrical Resistance Heater

Both current and voltage drop in the heater must be measured to track the electrical energy dissipated in the heater. A power resistor with a 10-ohm resistance and 10-watt power rating is placed in series with the power supply and resistance heater. By measuring the voltage across this resistor with a multimeter, the current through the heater can be calculated using Ohm's Law $V = IR$. A second multimeter measures the voltage drop across the heater. From these two pieces of information, voltage, current,

and $P = VI$, the electrical power dissipated as heat in the heater can be accurately calculated. Figure 3-1 depicts a schematic of the test circuit.

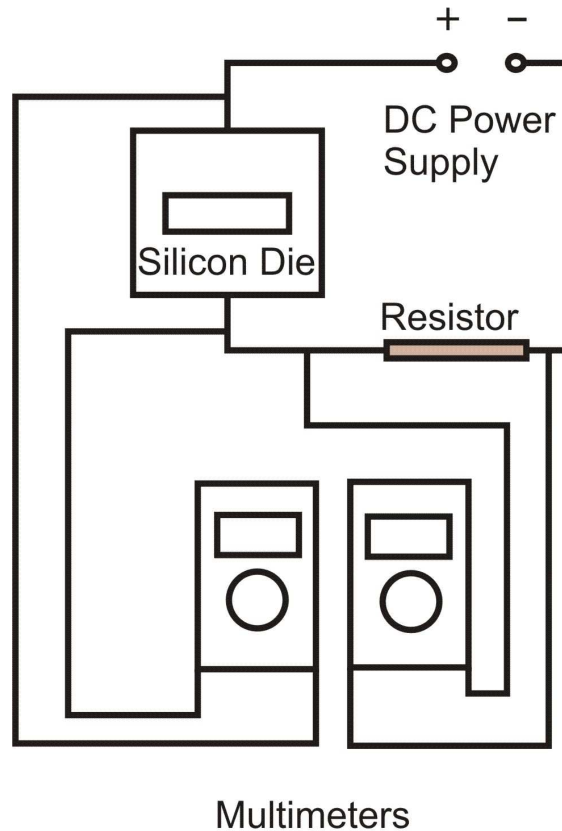

Figure 3-1: Power In Test Circuit

3.3 Energy Conducted Across Membrane

The heat flux conducted across the membrane is determined using Fourier's Law along with two temperatures taken at different radii by two annular RTDs. These two temperatures are subtracted to get the radial ΔT across the membrane.

$$q_r = \frac{2\pi L k \Delta T}{\ln(r_2 / r_1)} \tag{3-1}$$

The constants used in this equation are k, the thermal conductivity of silicon (k= 153 W/mK) L, the thickness of the membrane (L =2 μm), and r_1 and r_2, the respective radii of the temperature measurements from the center (r_1 = 1.7 mm r_2= 2.35 mm).

Two RTDs are required for the overall energy balance to determine the radial temperature profile of the membrane. The RTDs measure temperature by changing in resistance as temperature changes. The resistance is measured and compared to a calibration curve, correlating the RTD resistance to temperature.

The RTD design consists of a serpentine of platinum lines connected to a platinum electrode.

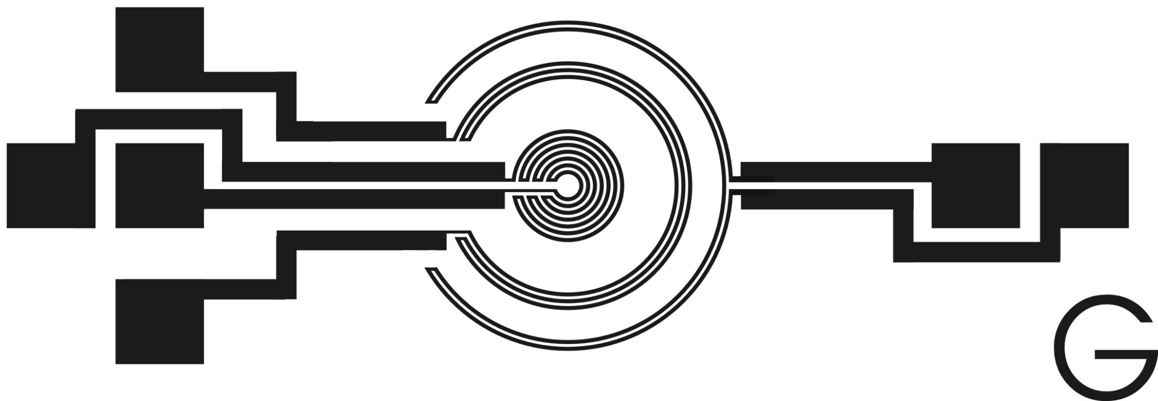

Figure 3-2: 5mm Heater/Dual RTD

Figure 3-2 shows the standard 5mm platinum heater/dual RTD. The center circle is the platinum resistance heater, connected to the two inner electrodes on the left. The resistance of the heater is relatively high, approximately 500 Ω, ensuring that the heat is dissipated on the membrane and not in the resistance heater leads. The heater and both inner and outer RTDs are made of 50 micron wide lines with 50 micron wide gaps in between. These dimensions are printable at WSU on a standard transparency but push the printing abilities to their current limits.

A Wheatstone bridge and calibration curve are used to convert the RTD resistance, or corresponding voltage, to temperature. The Wheatstone bridge consists of four resistors, a constant voltage input, and a voltage gage, in this case a multimeter.

Two of the resistances are known, one is variable, and one is to be measured. The circuit is balanced first using the variable resistor. The multimeter measuring across the circuit will read zero when the circuit is balanced. If the resistance of any of the four elements changes, there will be a voltage across the multimeter. This causes the multimeter to become an indicator of the balance of the circuit. When using the Wheatstone bridge in an experiment, a dc current is applied and the variable resistor is modified until the multimeter reads zero.

3.4 RTD Testing Box

To house the Wheatstone bridge circuits for protection and ease of transportation, a simple plastic box was constructed. The box is large enough to house two bridge circuits, one for each RTD, and all the components needed to operate them. Each circuit has inputs for the voltage signal from the RTD, outputs to an outside measuring device, two potentiometers for zeroing the circuit, an outside dc power source, and a set of four nine volt batteries to power the amplification chip. Because the signal from the RTDs was so small, often times smaller than the level of noise in the system, the amplification chip was used to magnify the signal to a level the was easier to read. Any time RTD measurements were taken; the testing box was hooked between the RTD and measuring device such as a multimeter or LabVIEW. This includes RTD calibrations as well as testing.

3.5 RTD Calibration

The voltage change of the RTD as temperature changes must be calibrated. A hot water bath, thermometer, and RTD testing box are used for the RTD calibrations. First, a wick heater RTD die is placed in a carrier and checked that all the wires are properly

contacted with electrodes. The carrier is then immersed in a bath of de-ionized water and the four RTD wires are connected to the RTD box. The outputs are connected to multimeters along with a multimeter that is directly connected to the heater probes. This is also set to voltage and measures the voltage change across the heater during the calibration. The bath of water with carrier is placed on a hotplate with a thermometer immersed in the liquid. A Corning hot plate is used with a magnetic stir bar. The carrier is placed on an acrylic ring inside the DI bath with the stir bar in the center of the ring. This allows for even stirring of the fluid but does not disturb the carrier. The heat and stir bar are both set to 6 and the voltage of the RTDs and heater are recorded as the temperature increases.

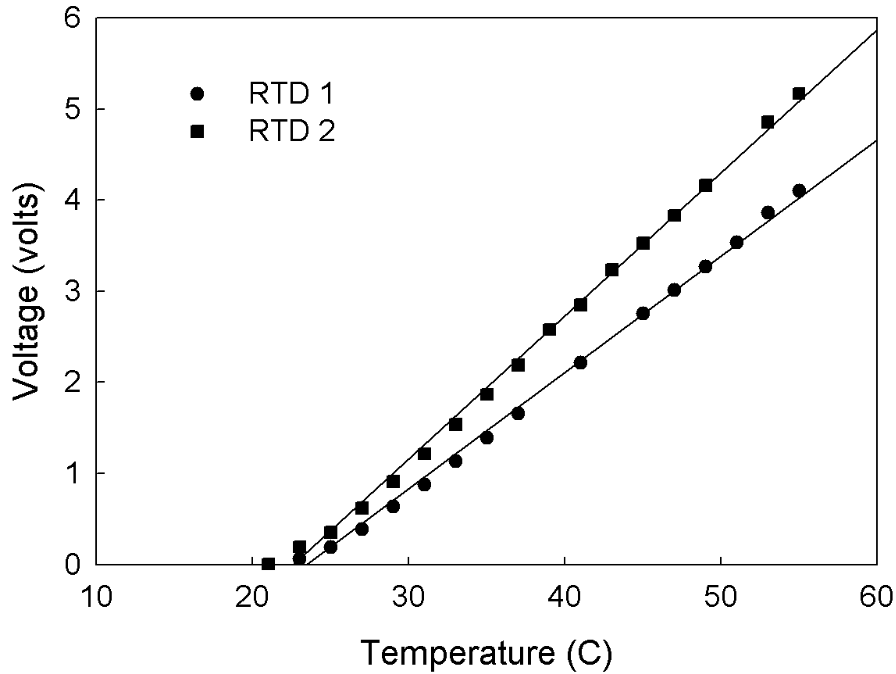

Figure 3-3: RTD Calibration Curve 966I

Figure 3-3 shows a typical RTD calibration curve with the increase in voltage from the bridge circuit corresponding to temperature increase. The equation of these two lines is used to relate temperature and voltage.

The RTD design met very specific criteria. The length of the platinum traces determines the overall resistance of the RTD. A resistance that is too low or too high will be out of range of the Wheatstone bridge. Both RTDs (along with the heater) were designed to have a resistances of approximately one half kilo-ohm. A second important aspect of the design is the RTD placement on the membrane. The RTDs must be far enough apart to register a difference in temperature. The evaporator is designed so that the liquid vapor interface for an evaporation test occurs between the heater and the first RTD. This ensures that the measured temperatures will not be affected by one RTD being wet and the other dry. Ideally, to satisfy these conditions, a very large membrane would be used to allow large spacing between the heater and first RTD. This was not possible however, since die size was limited to 10mm by 16mm. Furthermore, the evaporation experiment requires the use of an o-ring outside the membrane. As a result, there must be enough room for the o-ring on the edge of the die to seal working fluid to completely encircle the membrane. These experiments led to a membrane size of five or six millimeters. Both of these membrane sizes were used. The RTD was also designed in a circular shape to give accurate temperature measurements by maintaining radial symmetry along the membrane.

3.6 Energy Carried by Evaporation

Finally, the amount of fluid evaporated must be determined to give a complete energy balance. Measuring the evaporation rate enables accounting for energy carried

away by evaporation of the working fluid. The goal is to equate the sum of the energy across the membrane and the energy into evaporation to the energy put into the system. Like the previous experiments, the evaporation experiment tracks heat flux using the two RTDs and energy in using the test circuit. A twofold approach is used to track the energy carried away by evaporation of the fluid. First a reservoir of fluid is created using two o-rings and an acrylic carrier.

Second, the evaporation rate is tracked using a scale. The reservoir supplies the evaporator with a continuous amount of fluid. The square carrier made of a top and bottom acrylic piece hold both the heater die and fluid to evaporate. The carrier has four screw holes to secure the two pieces together and probes bonded into the carrier with epoxy. This allows for electrical contact to the heater and RTDs as well as preventing fluid from evaporating out around the probe holes. It also has a fill hole for fluid and a hole over the membrane to allow for evaporation. A set of two o-rings is used to control the amount of fluid that evaporates and ensure that the wicks are continuously delivering fluid. The first o-ring completely encircles the entire heater die. It sits in between the two carrier halves and is held in place by the compression of the carrier screws. The function of this o-ring is to enclose the fluid in the carrier and keep it from leaking out. The second o-ring sits between the top carrier and wafer die and encircles the heater and RTDs but does not interfere with the electrodes. It is important to note that the heater and RTDs are covered in wick channels and the o-ring will sit on top of these channels. This will effectively leave small gaps under the o-ring and will allow the capillary pumping force of the wicks to pull fluid into contact with the heaters. This allows for a constant,

steady amount of fluid to continually be pulled from a reservoir into contact with the heater. The experimental setup is depicted in Figure 3-4.

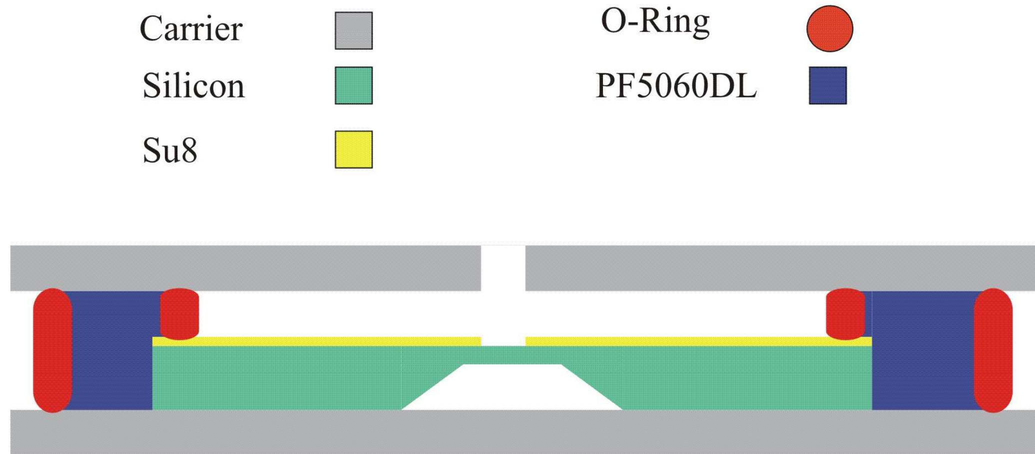

Figure 3-4: Evaporation Experiment Schematic

The combination annular/radial wick pattern is used in the evaporation experiments, depicted in Figure 2-9.

The evaporation rate is tracked using a very sensitive scale. The assembled carrier is placed on the scale at the beginning of the experiment. The total weight of the evaporator, carrier, and reservoir of working fluid is recorded. Next, electric power is put into the system. Weight readings are taken periodically (5 minute intervals) over the experiment to monitor the continual decrease of fluid through evaporation. At the end of the experiment, the rate of change of the weight of the carrier, evaporator, and reservoir of working fluid is taken to be the evaporation rate of fluid.

An Acculab VI-1mg digital scale with milligram accuracy is used to determine evaporation rate over the duration of the experiment. As the fluid evaporates, the carrier becomes lighter and registers less weight on the scale. Monitoring the weight change

gives overall mass of refrigerant evaporated. Knowing the latent heat of vaporization, allows the calculation of energy carried by evaporation of fluid. If the energy required to evaporate the known amount is close to the energy that went into the system, the efficiency of the heater is relatively high and almost all energy is used directly towards evaporation. If there is a large discrepancy between energy in and energy to evaporate, the energy is going elsewhere. This situation is less than ideal. It indicates less evaporation and a poor overall evaporator efficiency.

Both steady state and transient tests are conducted. A steady state test has the power on the entire duration of the experiment. RTD voltages, as well as the voltage across the heater and resistor, along with the scale reading, are recorded every five minutes. In contrast, a transient test yields voltages that change very rapidly. LabVIEW provides a signal output for the TTL circuit, which then controls the signal to the resistance heater on the evaporator. LabVIEW also records all the necessary voltages every five minutes.

3.7 Visualization

A temperature gradient forms across the membrane since the resistance heater heats the center of the membrane while working fluid wicks in from the outside edge. Controlling the amount of heat dissipated in the resistance heater can vary this temperature gradient. A liquid-vapor interface thus forms somewhere between the resistance heater and the outer circumference of the wick. The most desirable location of the liquid-vapor interface is between the heater and first RTD. This location ensures that the wicks are able to deliver fluid to the membrane and that both RTDs are covered with

fluid. A visualization of the experimental setup during operation gives the location of the liquid-vapor interface.

A TSI Particle Image Velocimetry (PIV) camera was hooked to a Questar QM1-10126-MKIII long distance microscope to facilitate visualization of the liquid vapor interface. It allowed viewing of the evaporator as it ran either transiently or steady state to visually determine the location of the liquid vapor interface. The lighting was the most difficult aspect of the visualization. The best results came from lighting the membrane from above and imaging from below.

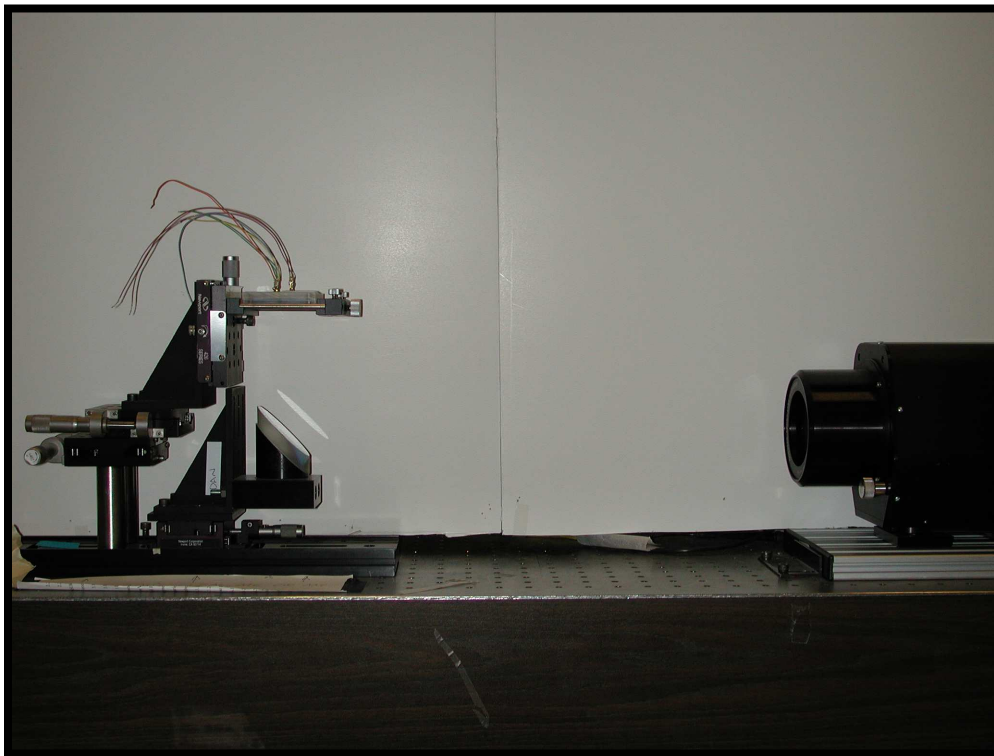

Figure 3-5: Visualization Setup

The visualization setup shown in Figure 3-5 consists of three main parts, each an assembly of other components. These are the camera, carrier jig, and light source. The camera is mounted on a sled along with the optical microscope, shown on the right of

Figure 3-5. The camera has a Nikon F (bayonet) mount and is connected to the microscope through a series of Questar extension tubes and "insertion rings." Inside these tubes are Barlow lenses (1.5x or 2x) used for extra magnification. The location of the lenses is variable, from right inside the back of the microscope, to directly in front of the camera, depending on the desired image. Multiple lenses can also be used for higher magnification although the image quality may suffer. The lenses are mounted by screwing the inside of the insertion ring onto the back of the Barlow lens. The lens is then compressed in between two extension tube pieces or one piece and either the camera or the long distance microscope. The carrier jig is assembled on another sled and placed approximately 23.5 inches from the camera and microscope, seen on the left side of Figure 3-5. There is a 90 degree angled mirror that is mounted on an x-y stage that is then mounted onto the sled. This mirror is used to see the membrane from the beneath. Behind the mirror is a jig that is mounted on the same sled and houses the carrier. The carrier lays flat and is attached to an x-y-z stage. This allows for adjustments in the x-y direction to aid in alignment with the mirror but also in the vertical z direction to change the focal length. This helps to fine tune the focusing of the image.

The membrane is lit from above with an adjustable fiber optic light. This light is placed directly over the open hole in the carrier and held in place by a clamp mounted on a separate post. The light by itself does not have the contrast to illuminate the wicks. Yellow tissue paper was placed in between the light and the carrier to act as a filter. Use of the tissue paper filter immensely improved overall image quality and gave good images of the wick and liquid/vapor interface.

3.8 Experimental Uncertainty

The uncertainty of the results revolves around the three elements of the energy balance. The measurements for the power in, flux across membrane, and evaporation are all subject to their respective inaccuracies. These uncertainties include the equipment used to sample the data, the data analysis, and hardware components of the experiment. Measuring the power dissipated in the resistance heater required multimeters and a power resistor. The voltage across both the heater and resistor were measured with Fluke 189 true RMS multimeters. These multimeters have an uncertainty of .025%. The uncertainty was determined using root of the sum of squares (RSS).

$$w_R = \left[\sum_{i=1}^{n} \left(w_{xi} \frac{\partial R}{\partial x_i} \right)^2 \right]^{1/2} \qquad (3\text{-}2)$$

RSS gives the confidence level of the result (R) in terms of the uncertainties of the components (x_i). Since the power into the heater is a function of the current $P = VI$ and the current is a function of the voltage and resistance $I = V/R$ this equation was used to calculate the uncertainty of the current and then power calculations. Both of these were based on voltage measurements by the Fluke multimeters. These were used to sample the voltage across the heater, resistor, and resistance of the resistor. Because of the very high accuracy of these multimeters, the current and then power calculations have uncertainties lower than 1% of the measured value and were not considered as a significant contributor to error.

Measuring the flux across the membrane is the next of the three components that went into the energy balance. Equation (3-1) was used to calculate the flux and is based on the thickness of the membrane, temperature measurements at two points on the

membrane, radius of these points, and thermal conductivity of silicon. The thickness of the membrane includes the silicon membrane itself as well as the layer of silicon oxide grown after the membrane has been etched. The value of 2 microns was determined to have an uncertainty of 10% of the overall thickness or ± 0.2 microns. The uncertainty of the RTD measurements was calculated using the standard deviation of the residuals (S) and students t distribution (t) at a 95% confidence interval, shown in equation 3-3.

$$\mu = \bar{x} \pm t_{\alpha/2} \frac{S}{\sqrt{n}} \tag{3-3}$$

The other values in equation 3-3 are the number of data points (n), the sample mean $\bar{x}$, and μ, the population mean. The result of this calculation was a $\pm .37$ °C confidence interval. When subtracting these two temperatures to get a ΔT, the uncertainties of the individual temperature measurements are added. This yields a ΔT uncertainty of approximately $\pm .75$ °C. The measurement of the two RTD radiuses comes from knowing their location on the photomask. The RTD masks were printed at Washington State University. The printing technology is limited and various print attempts have shown that the mask dimensions such as thickness of a line are accurate down to 20μm. Features smaller than 20μm run together. This error is less than 1% of the RTD distance from the center of the membrane and was therefore not considered as a contributor to overall uncertainty. Finally, the overall uncertainty of the heat flux is a function of all the contributing factors and is 10% of the resultant value.

The last component to the energy balance is the evaporation. The Acculab scale was used to measure the mass change of the carrier. Several measurements were taken of

a 100 gram calibration weight to determine the precision error of the scale. The precision index S_x was calculated using equation 3-4.

$$S_x = \left[\frac{\sum_{i=1}^{n} \left(x_i - \bar{x} \right)^2}{n-1} \right]^{1/2} \tag{3-4}$$

The precision limit was then calculated using S_x and equation 3-5:

$$P_{xi} = tS_x \tag{3-5}$$

where t is the Student's t distribution and is a function of the confidence level and degrees of freedom. In this case the confidence level was 95% and the degree of freedom was 62, the number of data points minus one. This yielded a confidence interval of ± 4.24 mg. A typical evaporation experiment lost approximately 150 milligrams to evaporation leaving the uncertainty to be 2.8%.

CHAPTER 4 PROCEDURES

4.1 Experimental Procedures

Both the evaporation and heat conduction experiments follow the same basic experimental procedures. The first step after fabrication, wafer dicing, and RTD calibration is to assemble the evaporator in its carrier. The evaporator die is placed on a semiconductor tape pad and aligned so that its membrane is above the hole in the bottom carrier and below the hole in the top. Special care must be taken to ensure all the probes are in contact with the proper electrodes.

Once aligned, the outer o-ring is placed on the acrylic around the die pad and die and the inner o-ring is placed on the die, just outside the membrane. The o-ring must not touch the membrane or it will break the membrane when the carrier is clamped. At the same time, the o-ring must be centered on the wick pattern so that the fluid will be able to wick underneath. Finally, the two carrier halves are clamped together until a flat line can be seen around both o-rings. This indicates that there is enough pressure to give a tight seal. If the carrier is not clamped tight enough, the working fluid will leak out during the experiment. If the carrier is clamped too tight, the die may break from the pressure.

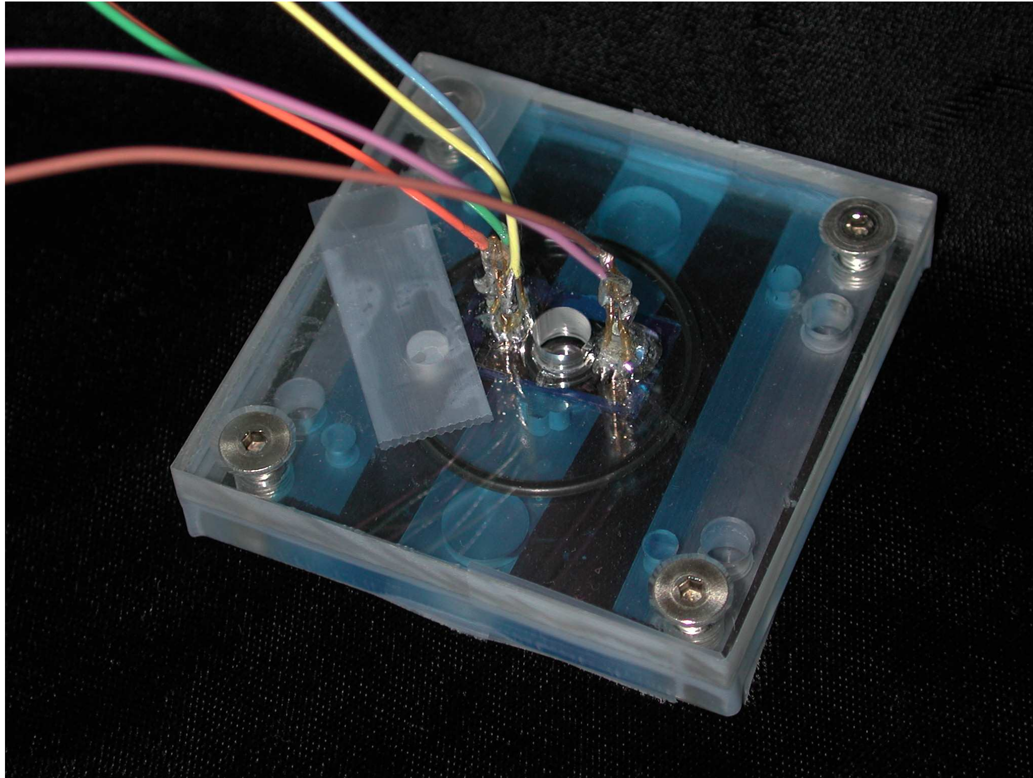

Figure 4-1: Assembled Carrier

Figure 4-1 shows a fully assembled carrier with die, o-rings, and connection wires. At this point, the heater die is ready for any experiment, calibration, or visualization.

4.2 Steady State and Transient Heat Conduction Experiments

A heat conduction experiment is used to verify the energy balance on the evaporator without any evaporation. This test gives an indication of the value of the dual RTD method to measure heat conduction across the membrane. The goal is to measure both the energy dissipated by the heater and the energy conducted across the membrane. These two energy terms should be equal. In the steady state heat conduction experiment, the silicon die with membrane, heater, and RTDs is placed in its acrylic carrier. The system is left dry. No working fluid is added to the carrier reservoir. The conductive flux and the power into the heater are then measured using the test circuit, power supply,

and multimeters hooked to the RTDs. First, the power is turned on for ten minutes to allow the system to reach steady state. Multimeters are read every two minutes.

The transient heat conduction experiment is much like the steady state heat conduction experiment. However, in this experiment, the voltage across the heater is pulsed instead of continuously on. This procedure gives a pulsed heat input to the heater and is closer to the actual operation of the heater in a P^3 engine than a constant heat source. The pulsed signal is made possible by hooking a TTL circuit in series with the heater and power supply.

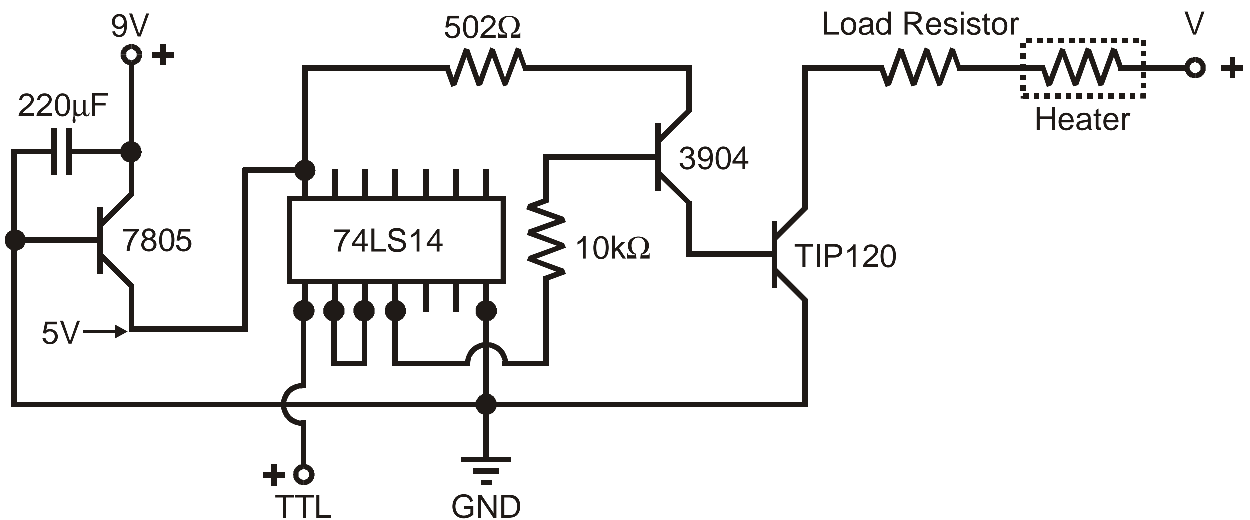

Figure 4-2: Schematic of TTL Circuit, Courtesy S. Whalen[35]

A diagram of the TTL circuit is shown in Figure 4-2. An outside signal is used to control pulse parameters such as frequency and duty cycle. A function generator virtual instrument from LabVIEW is used to control the pulse parameters. The function generator is hooked to the TTL (+) and GND. A range of frequencies and duty cycles are used to test the heat conduction response of the membrane. With any of the pulsed signals the multimeter cannot be used for voltage measurement because its time response

is too slow. Since the multimeters are not sufficient for the transient test, a software package called LabVIEW was used to both measure voltages as well as control the TTL. Two separate virtual instruments were used to stream the four measured voltages (2 RTDs, resistor, heater) to a spreadsheet for later analysis as well as output the signal for the TTL. Sampling at 2500 samples per second provided adequate time to capture the short heat pulses by the heater and subsequent response from the RTDs. The power into the heater and the conductive flux across the membrane can then both be integrated to obtain energy.

4.3 Steady state and Transient Evaporation Experiments

To begin an evaporation experiment, the carrier is placed on the scale and the probes are hooked to the RTD box. The RTD box is plugged into the wall with 1.5 V 700mA power adapters. The box is then zeroed and the RTD output values are recorded along with the scale reading. The carrier is then removed from the scale, filled with PF5060DL, and sealed with scotch tape over the fill hole. Next the carrier is placed back on the scale and the new RTD/scale values are recorded. The timer is set for 5 minutes and data is taken every 5 minutes until the carrier is dry or a sufficient trend has been established. A transient test uses LabVIEW to both run the TTL and take the RTD, heater, and resistor voltages. LabVIEW procedures are documented in Appendix B. The output for the TTL is run for the duration of the experiment. The inputs are taken every 5 minutes for just a few pulses. These data are stored in a temporary memory buffer that is exported to Excel every 5 minutes and then written over with new data. A steady state test can use multimeters to sample all the required voltages instead of LabVIEW and does not require the use of the TTL. A conductive flux experiment is essentially the same for

both transient and steady state. However, the conductive flux experiment does not require the use of a scale since no fluid is being evaporated.

4.4 Visualization Procedures

To visualize liquid in a wick, a PIV camera is connected to a pulse synchronizer. First, an appropriate focal length is found. A simple way to find the appropriate length is to print text at 1 or 2 point font and then tape it to the carrier face. The paper is easily backlit and the focal distance can then be adjusted using the screw on the bottom of the long distance microscope until the text comes into view. The micrometer on the z-axis stage then provides fine adjustment until the image attains the best focus. Insight software is used to process the images.

For a steady state test, the power supply is hooked to the heater. The voltage is varied while the Insight software is set to the Free image capture setting for the exposure mode and the continuous image capture setting for the capture mode. Once the liquid vapor interface is to be imaged, the image settings are changed to single and hitting the Begin Capture icon captures an image. This image is then used to identify the liquid vapor interface position as a function of voltage in.

CHAPTER 5 RESULTS/ANALYSIS

5.1 Steady State Heat Conduction

The first of four experiments was the steady state heat conduction experiment. This test was used to verify that the dual RTDs are a valid measure of heat conduction rates. A successful energy balance will equate the energy dissipated by the resistance heater to the energy conducted across the membrane. The combination radial annular wick patter shown in Figure 5-6 was used in all of the following experiments. The resistance of the heater was 611 Ω. This experiment was run with no fluid on the membrane. Three different values of power were dissipated into the heater: 35mW, 63mW, and 96mW. The results are plotted in Figure 5-1. The x-axis shows power dissipated in the heater. The y-axis shows the thermal power conducted along the membrane and as measured by the two RTDs. The solid line in Figure 5-1 below represents the case where all power dissipated in the heater is conducted radially out from the membrane.

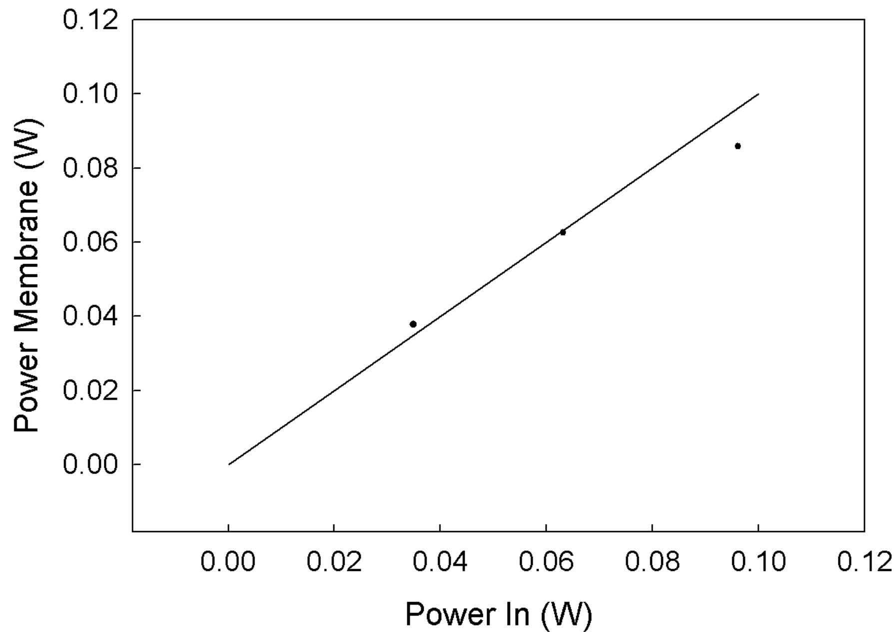

Figure 5-1: Steady State Heat Flux 5,7,9 Volts

At the lower power, heat conducted out is slightly higher than heat in. Around 60mW, heat in equals heat out along the membrane. At 100mW heat in is slightly higher than heat conducted out. The power measurements can be multiplied by the time interval to compare energy. For the case of 60mW in, the energy into the heater was 7.57J and the energy across the membrane was 7.5J over a two-minute time interval. This gives a 1% discrepancy between the two values (at 60mW). The temperatures measured by RTD1 and RTD 2 were 46°C and 35°C, respectively.

5.2 Transient Heat Conduction

The next experiment is the transient heat conduction experiment. Much like the steady state conduction experiment, the transient heat conduction experiment has no fluid on the membrane. The power put into the heater is balanced against the power that goes

across the membrane by conduction. For the transient experiments, however, the power dissipated in the membrane heater is pulsed.

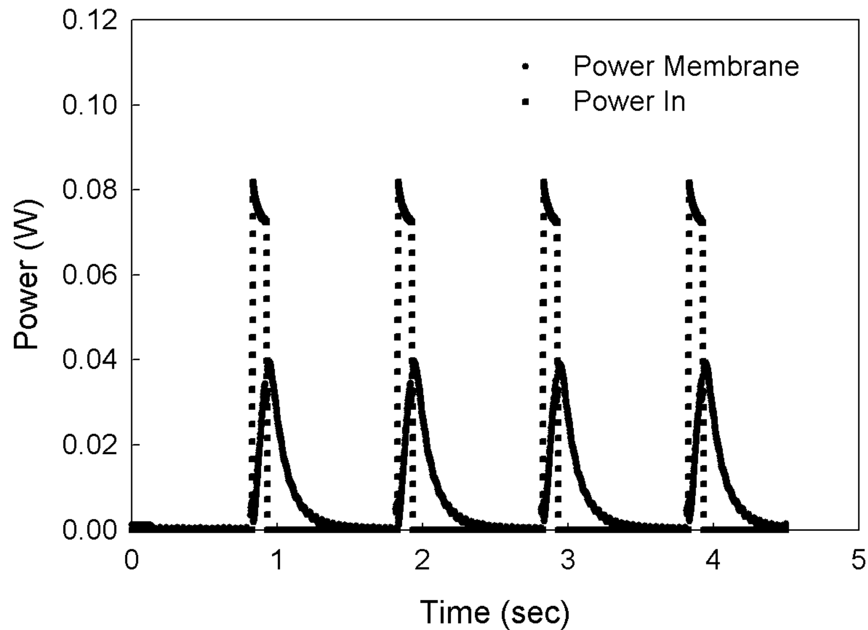

Figure 5-2: Transient Heat Flux 7 Volts

Figure 5-2 shows the pulsed power input to the evaporator and the corresponding heat conduction pulse across the membrane. The heat was pulsed at a frequency of 1Hz and duty cycle of 10%. The area under the two curves was calculated over a one second time interval using Excel. In this way the energy into the heater was compared to the energy conducted across the membrane. The energy dissipated in the heater for one second was .0075J. The energy conducted across the membrane was .0073J. This gives a 3.47% discrepancy between the energy in and the energy conducted out. The temperatures measured by RTD1 and RTD2 were 33°C and 26°C, respectively.

5.3 Steady State Evaporation

The focus of the steady state evaporation experiment was the accounting and balancing of the energy in, the energy conducted across the membrane, and the energy carried away from the membrane by evaporation. As with the other experiments, the combination radial annular wick shown in Figure 5-6 was used for the evaporation tests. Figure 5-3 shows the mass decrease as a function of time.

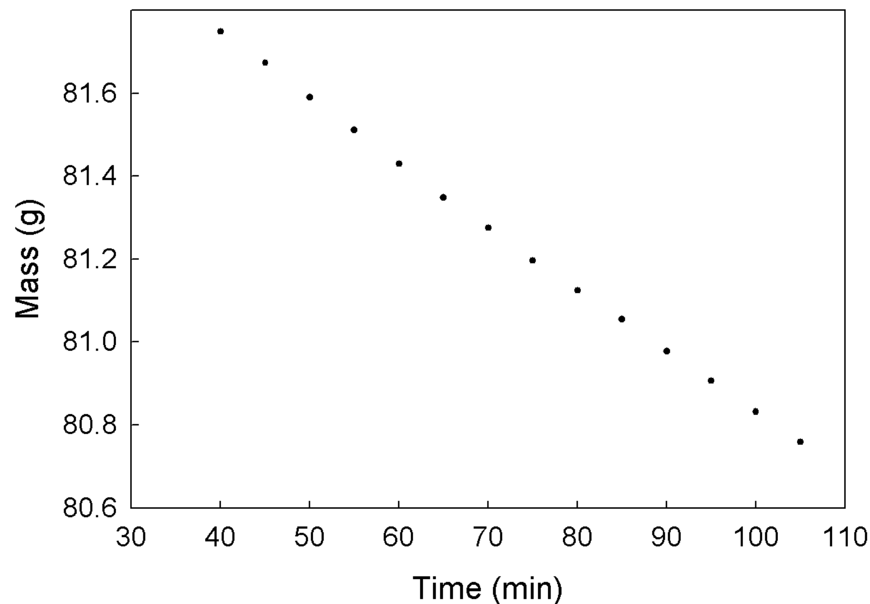

Figure 5-3: Steady State Evaporation 6 Volts

The rate of decrease of mass of working fluid was .0172 grams per minute. The experiment was run at a power in of 48mW. RTD1 and RTD2 measured temperatures of 40°C and 30°C respectively. The energy into the membrane over a 5-minute period was 14.47J. The energy conducted across the membrane was 17.2 Joules. The energy carried away by evaporation was 6.25 Joules. The energy conducted across the membrane and energy carried away by evaporation sum to an amount (23.45J) greater than was put in by the heater (14.47J). This discrepancy required further attention.

First, it was found that the working fluid evaporated from the evaporator even with no power to the heater. This background evaporation of PF5060DL must be taken into account. With a vapor pressure of 232 mmHg, PF5060DL evaporates relatively rapidly when left to the open atmosphere. For comparison, water has a vapor pressure of only 23.76 mmHg at 25 °C and evaporates much more slowly. As reported above, the experiment does not account for this background evaporation. Only the overall mass change is measured. Since, this approach is not entirely accurate, the background evaporation must be accounted for.

To account for background evaporation, an evaporation test was run with no power to the heater. The scale was measured at five-minute intervals as before. With no heat put into the system, the rate the working fluid evaporated could be measured to allow for a correction.

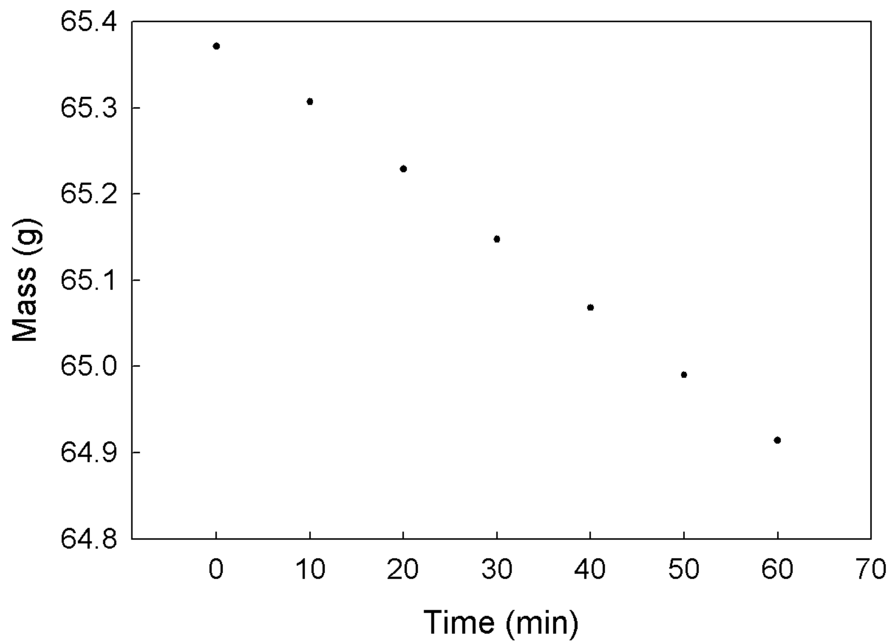

Figure 5-4: Zero Power Evaporation

Figure 5-4 shows the steady state, unheated evaporation from the carrier. The evaporation rate was .0077 grams per minute. This is .0385 grams for a 5-minute period. Subtracting the background evaporation from the total evaporation in the steady state evaporation experiment described above gives an adjusted energy of 3.36J going to evaporation instead of 6.25J. Table 5-1 gives a summary of evaporation mass rates and corrections used for both the steady state and transient evaporation experiments.

	Steady State Evaporation	Transient Evaporation
Evaporation Rate	0.0159 g/min	0.0131 g/min
Total Evaporation - 5 minute interval	0.079 g	0.067 g
Zero Power Evaporation (Correction Factor)	0.0385 g	0.0385 g
Corrected Evaporation	0.0405 g	0.0285 g

Table 5-1: Evaporation Summary

The second aspect of this experiment to examine is the power conducted across the membrane measured by the RTDs. Figure 5-1 shows that heat conduction along the membrane is over predicted by approximately 9% at a power input near 40mW. If 9% of the energy conducted across the membrane is subtracted from the measured value of the steady state evaporation experiment, the energy across the membrane goes down to 15.7J. That leaves the energy into the system still at 14.5J, the energy conducted across the membrane at 15.7J and the energy carried away by evaporation at 3.36J. The sum of energy conducted across the membrane and energy carried away by evaporation is 19J and has a discrepancy of 27% with the energy into the system. The efficiency of steady state evaporation is 23%.

5.4 *Transient Evaporation*

The transient evaporation experiments were conducted in the same manner as the steady state experiments. The only change was the pulsed heat input. The TTL was pulsed at a frequency of 1Hz and 50% duty cycle. This test most resembles what goes on inside the P^3 engine. Figure 5-5 shows the power in and corresponding heat pulse across the membrane as a function of time.

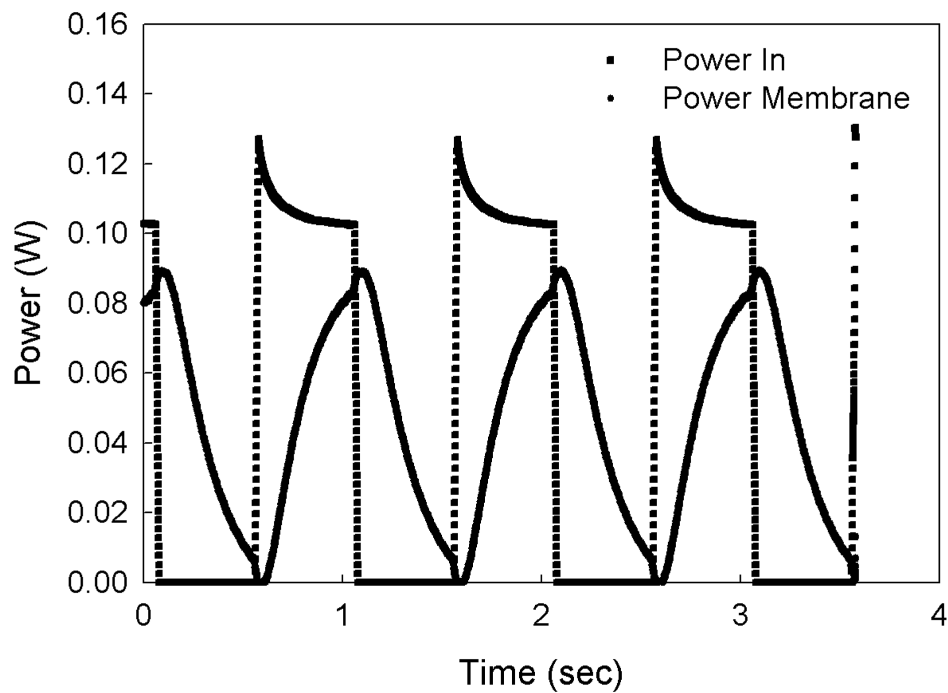

Figure 5-5: Transient Evaporation 10 Volts

The areas under the curves were integrated to get the energy dissipated into the heater and the energy conducted across the membrane. The scale gave the mass rate of evaporation and the energy carried away by evaporation. RTD1 and RTD2 measured temperatures of 42°C and 22°C respectively. The energy into the heater was 16.03J. The energy conducted across the membrane was 13.87J. The energy carried away by evaporation (adjusted to account for background evaporation) was 2.51J. In this

adjustment, .0385 grams of background evaporation was subtracted over a five-minute period from the total mass change recorded by the scale.

The sum of energy carried away by evaporation and energy conducted across the membrane is seen to balance within 2.11% of the energy into the system. The efficiency of the transient evaporation, the energy to evaporate fluid over the energy into the heater, is 15.66%. Table 5-2 provides a summary of the four experimental results.

	Steady State Flux	Transient Flux	Steady State Evaporation	Transient Evaporation
Energy In	7.6 J	0.0075 J	14.5 J 48 mW	16 J 53.4 mW
Energy Membrane	7.5 J	0.0073 J	15.7 J 52 mW	13.9 J 46.2 mW
Energy Evaporation	NA	NA	3.4 J 11 mW	2.5 J 8.36 mW
% Discrepancy	1%	3%	27%	2%
% Efficiency	NA	NA	23%	15%
Membrane Temperature (RTD1)	46°C	33°C	40°C	42°C
Membrane Temperature (RTD2)	35°C	26°C	30°C	22°C
ΔT	11°C	7°C	10°C	20°C

Table 5-2: Energy Balance Summary

5.5 Visualization Results

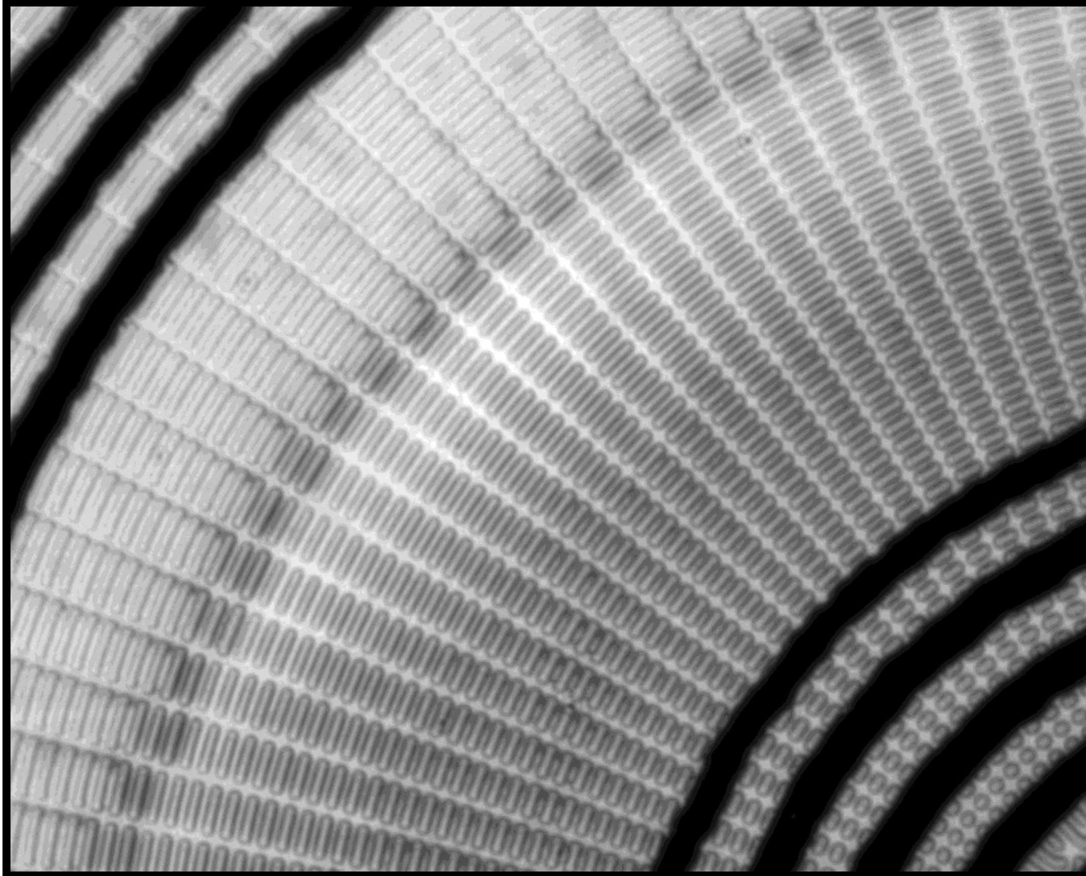

Figure 5-6: PIV Visualization 6.7 Volts 966I

Figure 5-6 shows a typical liquid/vapor interface for the wick pattern used in the evaporation experiments. The dark rings in the bottom right corner of the picture are the platinum heater. The corresponding rings in the upper left are the first RTD. The gray ellipses arranged radially around the heater are the SU8 wicks depicted in Figure 2-9. The circular dark/light disparity arcing around the picture in line with the RTD is the liquid/vapor interface. The channels on the right side of the interface are dry because of heat from the nearby platinum heater. The channels to the left are wet. This visualization successfully shows that during a steady state evaporation test, 75mW input to the heater will not push the liquid/vapor interface beyond the first RTD.

5.6 Background Evaporation Corrections

In an effort to eliminate the need for a background evaporation correction, several alternatives were explored. First, the entire experiment was run in a refrigerator to decrease the rapid evaporation from PF5060DLs very high vapor pressure. The low temperatures significantly affected the operation of the scale, however. The effect of the low temperatures on the scale made accurate measurements of mass impossible. Second, an effort was made to ensure the carrier was properly sealed. The probes were covered with epoxy. The carrier halves were sealed with tape. However even with these efforts, the fluid still evaporated fairly rapidly without any power input to the heater. Other fluids such as IPA and DI water could have been used but they were unable to wick with such small capillary dimensions.

Finally, a fluid with similar characteristics to PF5060DL but a much lower vapor pressure was sought. The use of a lower-vapor pressure working fluid was expected to give a lower evaporation rate and to eliminate the need for a correction factor. FC77, a refrigerant very similar to PF5060DL yet with a lower vapor pressure was found. The vapor pressure of FC77 is 42 mmHg at 25°C instead of the 232 mmHg vapor pressure for PF5060DL.[42] A zero power evaporation experiment was conducted with FC77 to compare the background evaporation of the fluid to that of PF5060DL.

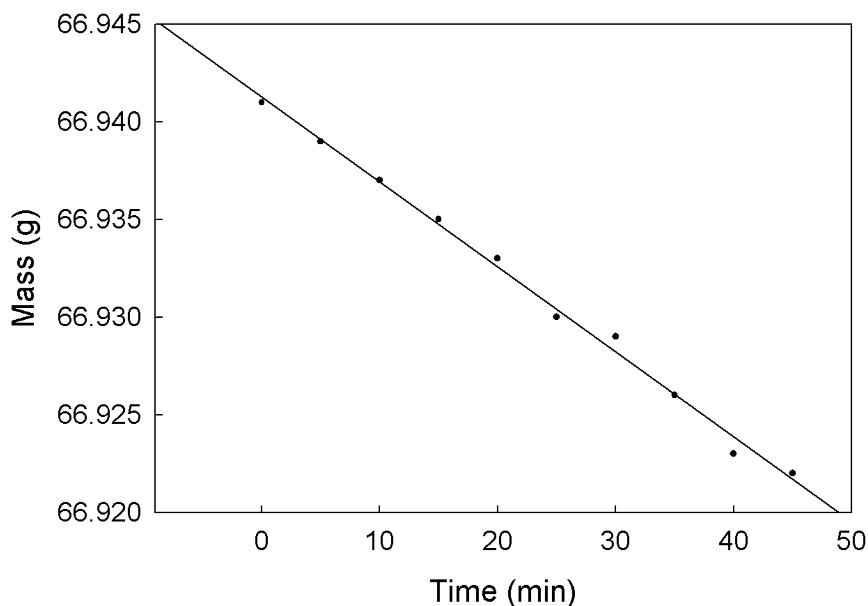

Figure 5-7: Zero Power FC77 Evaporation

Figure 5-7 shows the background evaporation experiment for FC77. The change in mass for FC77 without outside heating is shown plotted against time in minutes. The evaporation rate is 0.0004 grams per minute. This rate is almost twenty times less than the 0.0077 grams per minute background rate of PF5060DL. This decrease in background evaporation eliminates the need for the correction factor. Using FC77 instead of PF5060DL allows all energy into evaporation to be compared directly to energy put into the system by the heater.

A steady state evaporation test, performed like the previous tests except for the substitution of FC77, demonstrates this result.

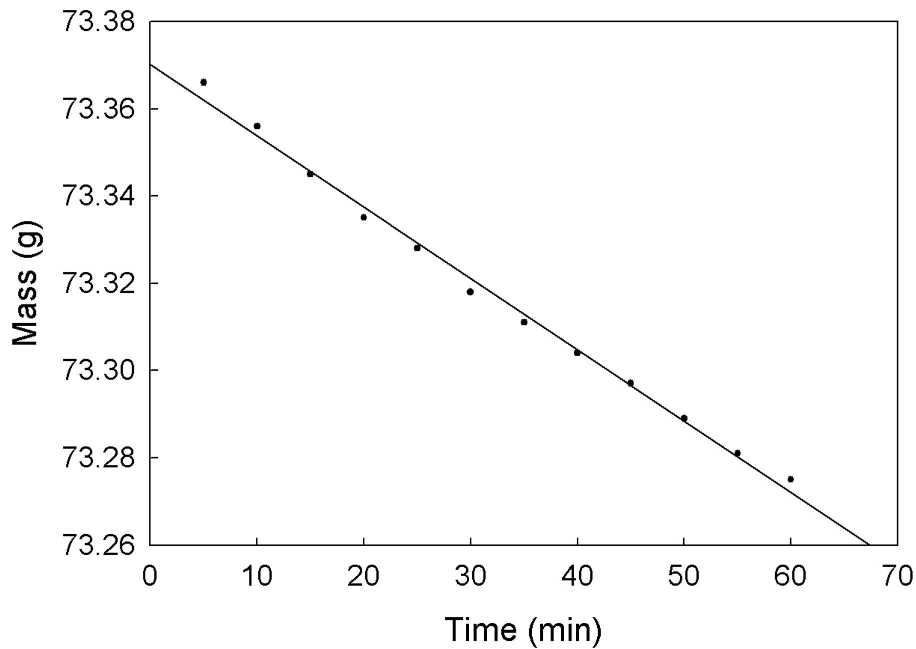

Figure 5-8: Steady State FC77 Evaporation 7 Volts

Figure 5-8 shows the steady state 64mW FC77 evaporation test. The evaporation rate is 0.0016 grams per minute and is 4 times greater than the unpowered background evaporation shown in figure 6-1. The energy conducted across the membrane is 19.68J. and the energy to evaporation is 0.69J. The energy into the system is 19.13J. The sum of the energy conducted across the membrane and the energy carried away by evaporation is 20.38J. The energy in balances the energy out within 6%. This test shows the success of the energy balance without corrections for background evaporation.

CHAPTER 6 CONCLUSIONS

6.1 Conclusions

The most important aspect of these experiments was to determine the efficiency of a micro capillary evaporator. The micro capillary evaporator in transient operation had an efficiency of 16%. The steady state evaporation efficiency was found was fount to be 23%.

For transient operation the 16% efficiency means that only 16% of the input energy is being used for evaporation and the remaining 84% of input energy was lost across the membrane. The evaporator's current use of input heat leaves significant room for improvement. The obvious improvement is to reduce the energy flux across the membrane to increase the energy to evaporate fluid. Membrane materials with lower thermal conductivities would decrease the conductive heat flux across the membrane and increase the energy to evaporate fluid.

Ideally the transient evaporation tests would have been run at a frequency and duty cycle very near the P^3 engine's operating point. The P^3 engine typically runs at around 10 Hz and 5-10% duty cycle. However, the power input at these settings was so small that it became difficult to get accurate data. At these settings, the inherent noise and uncertainty of the system was comparable to the measured power. In many cases the measured evaporation rate was less than the correction for the background, making the result questionable. For these reasons, the experiment was run at the higher duty cycle to increase the power in and bring the heat conduction and evaporation to reasonable values.

A correction factor proved to be necessary to make the energy balance work. A number of possibilities were explored to avoid implementing a background evaporation correction. The use of a lower vapor pressure working fluid FC77 proved successful.

APPENDIX A SU8 FABRICATION STEPS

- Clean wafer with five step process. Acetone, IPA, DI water, Acetone, IPA + canned air
- Place on hotplate at 200 °C for 5 minutes to remove any organics
- Spin coat the wafer with 2010 SU8 at 2000 rpm for 30 seconds for a 10 μm thickness
- Soft bake the wafer at 65 °C for 1 minute and immediately following 95 °C for 2 minutes
- Expose wafer using predetermined time for substrate and desired pattern
- Post exposure bake for 2 minutes at 65 °C and 3 minutes at 95 °C
- Let wafer cool for 5 minutes after baking
- Develop wafer using a full immersion in 2010 SU8 Developer for 3 minutes with strong agitation
- Rinse with IPA + canned air
- Cure on hotplate at 200 °C for 5 minutes

APPENDIX B LABVIEW PROCEDURES

LabVIEW is a programming language that uses graphical icons to create programs (called virtual instruments or VIs) instead of written code. It was used in all the transient experiments to sample the data at high speeds, send it to a spreadsheet for processing, and output a signal to control the TTL circuit. LabVIEW software is connected with real world instrumentation through a PCI 6052e board installed in a PC. The board is then hooked to a SCB-68 controller box that has sixteen analog input channels and two analog output channels. Each channel is configured in Measurement and Automation Explorer to accept or output certain voltage ranges and then the box is wired to the proper instrumentation. Two virtual instruments were used during these tests. The first was an adaptation of LabVIEW's example VI Simultaneous AIAO Buffer E-series. This VI simultaneously takes in and sends out analog data through memory buffers and is tailored to work with an e-series device. For transient tests, the VI was modified to only output a signal and was used to control the TTL circuit. Because this VI did not stream the data to a spreadsheet and could only hold a small amount in the memory buffer before being overwritten, it was not well suited to measure the voltages across the heater and RTDs. The front panel for this VI is depicted in Figure B-1.

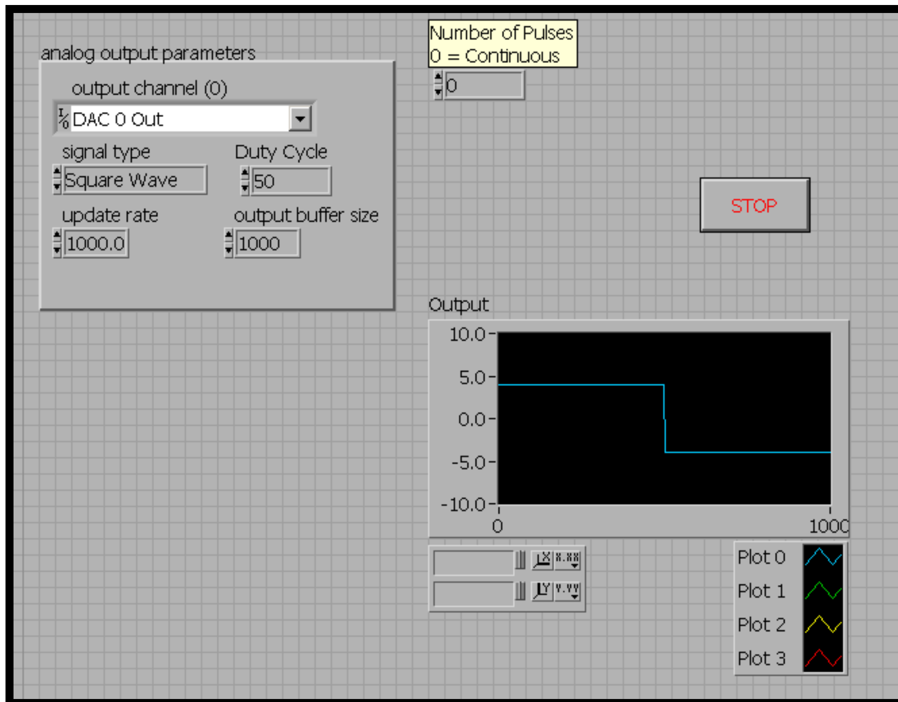

Figure B-1: LabVIEW Front Panel – Analog Out For TTL

Although this VI is relatively simple, there are a few key parameters to notice. The most important is the analog out parameters in the upper left corner. The output channel must be set to the properly configured channel that is wired in the controller box to the device. In this case, DAC 0 Out is the first of the two analog out channels that is wired to the TTL circuit board. This channel was previously configured in Measurement and Automation Explorer to match the correct pin assignments in the controller box. The rest of the analog output parameters control the signal. The signal type is set to square wave for a pulsed signal and the duty cycle is set to whatever percentage of the pulse is desired to be off. If a 10% duty cycle were desired, the duty cycle in LabVIEW would be set to 90. The update rate is the number of updates generated per second and the output buffer size is the number of updates the buffer will hold. Frequency of the signal is

update rate over output buffer size. The number of pulses will regulate how many pulses the VI outputs before it stops. A zero setting is continuous output.

For sampling the voltages across the heater, two RTDs, and power resistor, a LabVIEW example VI Continuous Acquisition to Spreadsheet File was used. This VI can sample multiple channels, store them in a temporary memory buffer, and stream them to a spreadsheet. This vi is depicted in Figure B-2.

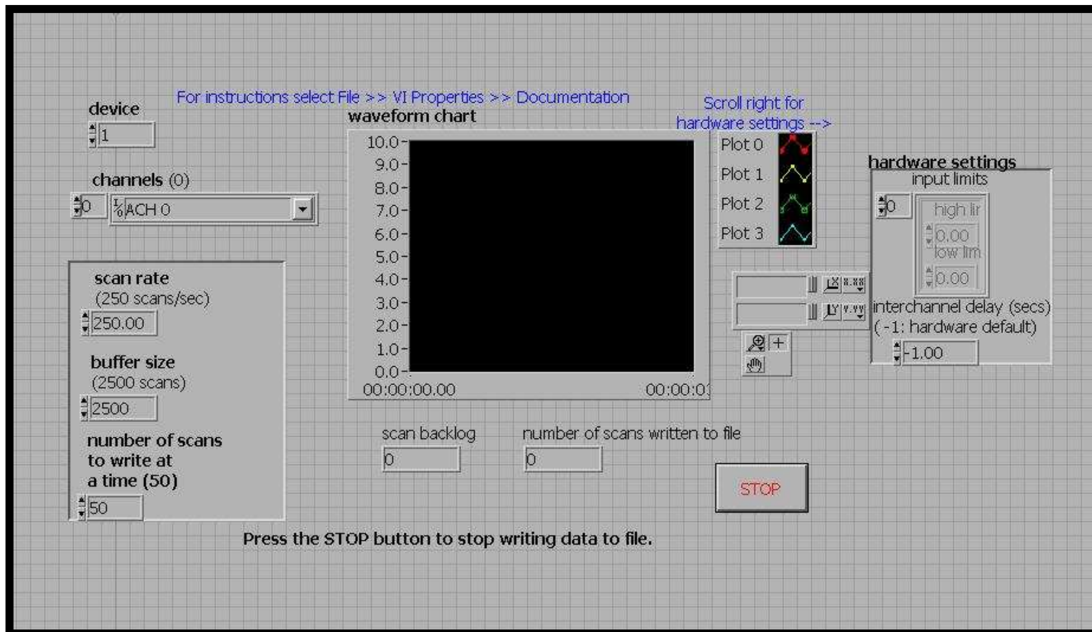

Figure B-2: LabVIEW Front Panel – Analog Input

The important parameters for this VI are the channels to be sampled and the scan settings, both on the left hand side of the VI. The data is displayed in the waveform chart in the center. The channel array can be configured for however many channels need to be sampled. Channel 0 is set to Analog Channel 0 (shown) 1 is set to Analog Channel 1 and so on. The scan rate used for the transient testing was 2500 samples/sec (default is 250). This gave enough resolution to see the signal but was not too much data to overload the buffer when run over just a few seconds. The

buffer size must be at least equal to the scan rate or data may be overwritten when the buffer fills.

References

[1] Paula, Greg , "MEMS Sensors Branch Out," *Mechanical Engineering* October 1996: 64

[2] DeGaspari, John, "MEMS' Rocky Road," *Mechanical Engineering* June 2002: 38

[3] Luanay, S., Sarte, V., Lallemand, M., "Experimental Study On Silicon Micro-Heat Pipe Arrays," *Applied Thermal Engineering* 24 (2004) 233-243

[4] Mallik, Arnab K., Peterson, G.P., Weichold, Mark H., "Fabrication of Vapor-Deposited Micro Heat Pipe Arrays as an Integral Part of Semiconductor Devices," *Journal of Microelctromechanical Systems* 4 (1995) 119-131

[5] Lee, Seri, "Optimum Design and Selection of Heat Sinks," *Eleventh IEEE Semi-Therm^{TM} Symposium* (1995) 48-54

[6] Saini, Manish, Webb, Ralph L., "Heat Rejection Limits of Air Cooled Plane Fin Heat Sinks For Computer Cooling," *2002 Inter Society Conference on Thermal Phenomena* (2002)

[7] Jia, W., Qiu, H.-H., "Experimental Investigation of Droplet Dynamics and Heat Transfer in Spray Cooling," *Experimental Thermal and Fluid Science* 27 (2003) 829-838

[8] Sabry, M.N., Djebedjian, B.O., Saleh, S.H., Mahgoub, M.M., "Modeling Heat Transfer and Liquid Flow in Micro-channels," *5th International Conference on Thermal and Mechanical Simulation Experiments in Micro-electronics and Micro-Systems* (2004) 511-518

[9] Benson, D.A., Mitchell, R.T., Tuck, M.R., Adkins, D.R., Palmer, D.W., "Micro-Machined Heat Pipes in Silicon MCM Substrates" *Multi-Chip Module Conference*, MCM-96, Proceedings, 1996 IEEE, 6-7 Feb. (1996) 127-129

[10] Ha, J.M., Peterson, G.P., "Capillary Performance of Evaporating Flow in Micro Grooves: An Analytical Approach for Very Small Tilt Angles," *Journal of Heat Transfer* 120 (1998) 452-457

[11] Ponnappan, R., "A Novel Micro-capillary Groove-wick Miniature Heat Pipe," *Proceedings of the Intersociety Energy Conversion Engineering Conference,* 2 (2000) 818-826

[12] Khrustalev, D., Faghri, A., "Heat Transfer During Evaporation on Capillary-Grooved Structures of Heat Pipes," *Journal of Heat Transfer* 117 (1995) 740-747

[13] Wu, D., Peterson, G.P., "Transient Experimental Investigation of Micro Heat Pipes," *Journal of Thermophysics* 5 Oct-Dec (1991) 539-544

[14] Longtin, J.P., Badran, B., Gerner, F.M., "A One-Dimensional Model of a Micro Heat Pipe During Steady state Operation," *Journal of Heat Transfer* 116 (1994) 709-715

[15] Ha, J.M., Peterson, G.P., "The Heat Transfer Capacity of Micro Heat Pipes," *Journal of Heat Transfer* 120 (1998) 1064-1071

[16] Peterson, G.P., Ha, H.B., "Theoretical Analysis of the Maximum Heat Transport in Triangular Grooves: A study of Idealized Micro Heat Pipes," *Journal of Heat Transfer* 118 (1996) 731-739

[17] Ha, H.B., Peterson, G.P., "Experimental Investigation of the Maximum Heat Transport in Triangular Grooves," *Journal of Heat Transfer* 118 (1996) 740-746

[18] Yu, J., Momoki, S., Koyama, S., "Experimental Study of Surface Effect on Flow Boiling Heat Transfer in Horizontal Smooth Tubes," *International Journal of Heat and Mass Transfer* 42 (1999) 1909-1918

[19] Bergles, A.E., Lienhard V, J.H., Kendall, G.E., Griffith, P., "Boiling and Evaporation in Small Diameter Channels," *Heat Transfer Engineering* 24 (2003) 18-40

[20] Pratt, D.M., Brown, J.R., Hallinan, K.P., "Thermocapillary Effects on the Stability of a Heated Curved Meniscus," *Journal of Heat Transfer* 120 (1998) 220-226

[21] Ma, H.B., Peterson, G.P., "The Minimum Meniscus Radius and Capillary Heat Transport Limit in Micro Heat Pipes," *Journal of Heat Transfer* 120 (1998) 227-233

[22] Ha, J.M., Peterson, G.P., "The Interline Heat Transfer of Evaporating Thin Films Along a Micro Grooved Surface," *Journal of Heat Transfer* 118 (1996) 747-755

[23] Chamra, L.M., Webb, R.L., "Advanced Micro-fin Tubes for Evaporation," *International Journal of Heat and Mass Transfer* 39 (1996) 1827-1838

[24] Shen, D.S., Mitchell, R.T., Dobranich, D., Adkins, D.R., Tuck, M.R., "Micro Heat Spreader Enhanced Heat Transfer in MCMs," *Proceedings of the IEEE Multi-Chip Module Conference,* (1995) 189-194

[25] Le Berre, M., Launay, S., Sartre, V., "Fabrication and Experimental Investigation of Silicon Micro Heat Pipes for Cooling Electronics," *Journal of Micromechanics and Microengineering* 13 (2003) 436-441

[26] Peterson, G.P., Duncan, A.B., Weichold, M.H., "Experimental Investigation of Micro Heat Pies Fabricated in Silicon Wafers," *Journal of Heat Transfer* 115 (1993) 751-756

[27] Hopkins, R., Fabhri, A., Khrustalev, D., "Flat Miniature Heat Pipes With Micro Capillary Grooves," *Journal of Heat Transfer* 121 (1999) 102-109

[28] Incropera, F.P., DeWitt, D.P., *Introduction to Heat Transfer* (New York: John Wiley and Sons, 1996)

[29] Olson, Benett, "Optimization of a Piezoelectric Membrane Generator," MS Thesis Washington State University (2002)

[30] Olson, Adam, "Processing and Properties of a Piezoelectric Membrane," MS Thesis Washington State University (2003)

[31] Tong, Alan, "Improving the Accuracy of Temperature Measurements," *Sensor Review* 21 (2001) 193-198

[32] Cho, Jeong-Hyun, "Electro-Mechanical Characterization of Piezoelectrics for MEMS Power," MS Thesis Washington State University (2004)

[33] Feng, R., Farris, R.J., "Influence of Processing Conditions on the Thermal and Mechanical Properties of SU8 Negative Photoresist Coatings," *Journal of Micromechanics and Microengineering* 13 (2003) 80-88

[34] Feng, R., Farris, R.J., "The Characterization of Thermal and Elastic Constants for an Epoxy Photoresist SU8 Coating," *Journal of Materials Science* 37 (2002) 4793-4799

[35] Whalen, S., "Demonstration of a MEMS Based Micro-Heat Engine and Characterization of the Thermopneumatic Actuation Mechanism With an Integrated Micro-Capillary Wicking Structure," Doctoral Dissertation Washington State University (2004)

[36] Zhang, J., Tan, K.L., Gong, H.Q., "Characterization of the Polymerization of SU-8 Photoresist and its Application in Micro-electro-mechanical Systems (MEMS)," *Polymer Testing* 20 (2001) 693-701

[37] Lorenz, H., Despont, M., Fahrni, N., Brugger, J., Vettiger, P., Renaud, P., "High-aspect-ratio, Ultrathick, Negative-tone near-UV Photoresist and its Applications for MEMS," *Sensors and Actuators* A64 (1998) 33-39

[38] Lorenz, H., Laudon, M., Renaud, P., "Mechanical Characterization of a New High-Aspect-Ratio Near UV-Photoresist," *Microelectronic Engineering* 41/42 (1998) 371-374

[39] Chantal, G., Khan, M., "SU8 Resist for Low-cost X-ray Patterning of High-resolution, High-aspect-ratio MEMS," *Microelectronics Journal* 33 (2002) 101-105

[40] Chang, H., Kim, Y., "UV-LIGA Process for High Aspect Ratio Structure Using Stress Barrier and C-Shaped Etch Hole," *Sensors and Actuators* 84 (2000) 342-350

[41] Cengel, Y.A., Boles, M.A., *Thermodynamics an Engineering Approach* (Boston: McGraw-Hill, 1998)

[42] 3M, "3M Fluorinert™ Electronic Liquids For Electronic Reliability Testing," www.3m.com